

# **Dark current mechanisms in amorphous Selenium X-ray imaging detectors**

Safayat-Al Imam

A Thesis

In the Department

of

Electrical and Computer Engineering

Presented in Partial Fulfillment of the Requirements

for the Degree of Master of Applied Science at

Concordia University

*Montréal* Québec Canada

© Safayat-Al Imam 2013

**CONCORDIA UNIVERSITY  
SCHOOL OF GRADUATE STUDIES**

This is to certify that the thesis prepared

By: Safayat-Al Imam

Entitled: "Dark current mechanisms in amorphous Selenium X-ray imaging detectors"

and submitted in partial fulfillment of the requirements for the degree of

**Master of Applied Science**

Complies with the regulations of this University and meets the accepted standards with respect to originality and quality.

Signed by the final examining committee:

\_\_\_\_\_ Chair  
Dr. R. Raut

\_\_\_\_\_ Examiner, External  
Dr. S. Rahaman, BCEE To the Program

\_\_\_\_\_ Examiner  
Dr. P. Valizadeh

\_\_\_\_\_ Supervisor  
Dr. M. Z. Kabir

Approved by: \_\_\_\_\_  
Dr. W. E. Lynch, Chair  
Department of Electrical and Computer Engineering

## ABSTRACT

# Dark current mechanisms in amorphous Selenium X-ray imaging detectors

Safayat-Al Imam

There has been a rejuvenated interest in amorphous selenium (a-Se) and its alloys as a photoconductive material in the arena of digital direct conversion flat panel X-ray image detectors (FPXI) for diagnostic medical imaging. However the a-Se photoconductive layer in FPXIs have to go through high applied field (up to  $10\text{V}/\mu\text{m}$ ) and makes one of the significant difficulties related to FPXIs by creating current in the absence of radiation known as dark current. This thesis deals with the effect of dark current under physics based theoretical modeling. The density of the defect states of deposited  $n$  layer of multilayer a-Se detectors are determined by analyzing the transient dark current behaviors. This analysis is important for the origin of time and bias dependent dark current being steady state. The improved model has been applied to alkaline doped  $n$ -layer and cold-deposited  $n-i$  based detectors and validated by the experimental results. This validation strongly supports the physical mechanisms responsible for the transient behaviour of dark current in the X-ray imaging detectors. The theoretical investigation of the density of states (DOS) of both  $n$ -layers (alkaline doped and cold deposited) link up the contribution between the trap concentrations and transient behaviour of the dark current.

The observation of impact ionization, which leads to avalanche multiplication on the amorphous selenium, has great impact on the low dose medical application such as general radiographic and fluoroscopic applications. However, the dark current can be high and very critical due to extremely high field and the avalanche nature of dark current. In this thesis, a physics-based analytical model for describing the transient and steady-state dark current is developed by considering bulk thermal generation, transient carrier depletion and avalanche multiplication. The model is validated by the published experimental results.

*To my loving parents*

*&*

*My brother*

## **ACKNOWLEDGMENTS**

First and foremost, I am thankful to Allah, the Almighty. I am indebted to my parents and my brother for their constant support. I would like to express my earnest gratitude to my supervisor Dr. M. Zahangir Kabir for his continuous guidance, inspiration, and financial support. I am grateful to my research colleague Khalid Sakib and Salman Moazzem Arnab. Also I would like to show my gratitude towards my cousin Dr Shahriar Al Imam and his wife Sayeeda Sultana and my little niece Tanisha Imam. Their inspiration and useful and friendly discussions motivated me a lot. Finally I am thankful to other members of my family for their concerns about my solitary life in Montreal.

# Table of Contents

LIST OF FIGURES.....	ix
LIST OF TABLES .....	xii
LIST OF ABBREVIATIONS .....	xiii
<b>CHAPTER 1:Introduction.....</b>	<b>15</b>
1.1 X ray (an electromagnetic wave) .....	15
1.2 Radiographic imaging.....	15
1.3 X-ray image detectors .....	17
1.4 Typical specification of digital X-ray system .....	19
1.5 Motivation .....	20
1.6 Research objective.....	23
1.7 Thesis outline .....	23
<b>CHAPTER 2:Background and Concepts .....</b>	<b>25</b>
2.1 X ray photoconductor.....	25
2.2 Amorphous materials .....	27
2.3 Amorphous selenium as an X-ray photoconductor .....	33
2.4 Practical a-Se multilayer detector .....	34
2.5 Amorphous selenium avalanche detector.....	36
2.5 Summary .....	39
<b>CHAPTER 3:Density of defect states of <math>n</math> layer of a-Se multilayer X-ray detectors .....</b>	<b>40</b>
3.1. Sources of dark current .....	41
3.2 Dark current in a-Se films .....	42

3.3	The model.....	44
3.4	Results and Discussion.....	49
3.5	Summary .....	56
<b>CHAPTER 4:Dark current mechanism in avalanche a-Se detectors .....</b>		<b>57</b>
4.1	Different types of structures.....	58
4.2	The proposed model for a-Se avalanche detector.....	62
4.3	The result and discussion .....	67
4.4	Summary .....	77
<b>CHAPTER 5:Conclusion, Contribution and Future Work .....</b>		<b>78</b>
5.1	Conclusion:.....	78
5.2	Contribution .....	79
5.3	Future work .....	80
References: .....		81

## LIST OF FIGURES

<b>Figure 1.1:</b> Schematics for digital radiography system	16
<b>Figure 1.2:</b> A simplified schematic diagram of the cross section of a single pixel with a TFT [2].	18
<b>Figure 2.1:</b> Various proposed models for density of states $g(E)$ as a function of energy. (a) DOS model for crystalline semiconductors (b) Mott's model (c) Marshall and Owen model.	29
<b>Figure 2.2:</b> The density of electronic states in a-Se as proposed by Abkowitz [16].	30
<b>Figure 2.3:</b> The density of electronic states in a-Se as proposed by Koughia [18][19][20]	32
<b>Figure 2.4:</b> A multilayer a-Se structure.	35
<b>Figure 2.5:</b> Process of avalanche multiplication (a) under non avalanche field (b) under avalanche field with more electron-hole pair due to impact ionization [23].	36
<b>Figure 2.6:</b> Schematic structure for observation of hole blocking mechanism	38
<b>Figure 3.1:</b> Origin of thermal generation current from the band diagram. The shaded area represents depletion of charge [28].	41
<b>Figure 3.2</b> (a) Schematic diagram of a multilayer a-Se based X-ray image detector. The electron-hole pairs are generated and then follow the electric field. (b) The relative magnitude of the field across the photoconductor is illustrated by F0 [31].	45
<b>Figure 3.3:</b> Dark current density of a-Se <i>n-i-p</i> sample as a function of time for four different positive applied fields. The symbols represent experimental data [8] and the solid lines represent the theoretical fit to the experimental data.	50
<b>Figure 3.4:</b> DOS distributions of deep states of n- alkaline doped n-layer by transient dark current analysis of Figs. 3.3	51

<b>Figure 3.5:</b> Dark current density in an n-i structure as a function of time at 10V/ $\mu\text{m}$ applied field. The symbol represents experimental data and the solid line represents the theoretical fit to the experimental data.	53
<b>Figure 3.6:</b> The DOS distributions of deep states in cold deposited n-layers by transient dark current analysis of Figure. 3.5.	54
<b>Figure 3.7:</b> The DOS distributions of deep states for different $n$ layers.	55
<b>Figure 4.1:</b> Schematic diagrams of a-Se avalanche detector structure (type I)	59
<b>Figure 4.2 :</b> (a) Schematic diagrams of a-Se avalanche detector structure (type II) (b) Energy band diagram model of the hole blocking structure [10].	60
<b>Figure 4.3:</b> Schematic diagrams of a-Se avalanche detector structure (type III)	61
<b>Figure 4.4:</b> Avalanche multiplication of holes and electrons under carrier injections and thermal generations $L$ is the a-Se layer thickness.	62
<b>Figure 4.5:</b> Impact ionization coefficient of holes as a function of electric field in a-Se.	68
<b>Figure 4.6:</b> Dark current density versus time. The symbols represent experimental data and the solid lines represent the theoretical fits [39].	69
<b>Figure 4.7:</b> Dark current density versus time for the a-Se avalanche detector structure of Figure 4.6 at extremely high fields [39].	70
Figure 4.8: Thermal generation current density versus electric field for three different mobility gaps of a-Se.	71
<b>Figure 4.9:</b> Hole injection current density as a function of electric field for (a) injection equal to thermal generation and, (b) injection equal to ten times thermal generation current at 50 V/ $\mu\text{m}$ . The dotted line represents the thermal generation current density for the mobility gap of 2.1 eV	72
<b>Figure4.10:</b> Dark current density as a function of electric field for two a-Se thicknesses. Dashed lines: hole injection current, dotted lines: bulk thermal generation current, and solid lines: total dark current.	73

**Figure 4.11:** Dark current density versus time in type II a-Se avalanche detector structure for three different fields. Symbols: experimental data, and solid lines: theoretical data for no tunneling and dashed line for  $\alpha=1.3\text{nm}$  74

**Figure 4.12:** Dark current density versus time in type III a-Se avalanche detector structure for two different fields. Symbols: experimental data, dotted lines: thermal and hole injection current and solid lines: theoretical fit to the experimental data [39]. 76

## LIST OF TABLES

<b>Table 1.1</b> Parameters for digital X-ray imaging systems for different major applications. The maximum energy of the emitted X-ray tube during the exposure is equal to the kVp value (data taken from [3].) Here kVp is peak kilo voltage which is the maximum voltage applied across the X-ray tube.	20
<b>Table 2.1.</b> Properties of stabilized a-Se (a-Se: 0.2-0.5% As +10-40 ppm Cl) films at room temperature (data taken from ref [13])	33
<b>Table 4.1</b> Comparisons of different parameters for various types of structures	61

## LIST OF ABBREVIATIONS

A/D	Analog to digital
Al	Aluminum
AMA	Active matrix array
AMFPI	Active-matrix flat-panel imagers
As	Arsenic
a-Se	Amorphous selenium
Au	Gold
CA	Cellulose acetate
CB	Conduction band
CeO <sub>2</sub>	Cerium oxide
Cl	Chlorine
CsI	Cesium Iodide
DOS	Density of State
DR	Digital radiography
EHP	Electron-hole pair
FPXI	Flat panel X-ray imagers
Gd <sub>2</sub> O <sub>2</sub> S	Gadolinium oxysulfide
ITO	Indium tin oxide
ppm	Parts per million
Pt	Platinum

RIL	Resistive interface layer
TFT	Thin film transistor
VB	Valence band
IIC	Impact Ionization coefficient

# **CHAPTER 1**

## **Introduction**

### **1.1 X ray (an electromagnetic wave)**

The discovery of X-ray by W. Röntgen approximately 117 years ago led the development of radiology and medical imaging. Produced by means of a vacuum tube or cathode ray tube, X-rays are electromagnetic waves with a relatively small wavelength (0.05-25nm) whereas the visible light wavelength is around ~600nm. When there is a high applied voltage across the tube (between the anode and cathode), the accelerated electron moves from cathode to the metal anode. The target is commonly made of tungsten for general radiography, but a molybdenum target is often used for mammography where lower energy X-rays are required. The loss of energy of the electrons due to impact is manifested as X-rays. These emissions of photon energies are determined by the electron energy levels. The unit of X-ray exposure is the Roentgen (R). It is a measure of X-ray radiation in terms of its ability to ionize air [1].

### **1.2 Radiographic imaging**

Within six months of its discovery, X-ray was being applied for the purposes of medical imaging and diagnostics and led to the development of a new branch of medical sciences known as diagnostic radiology. Figure 1.1 shows a typical imaging technique, in which

an object is placed between the X-ray sensitive image receptor (detector) and the X-ray source.

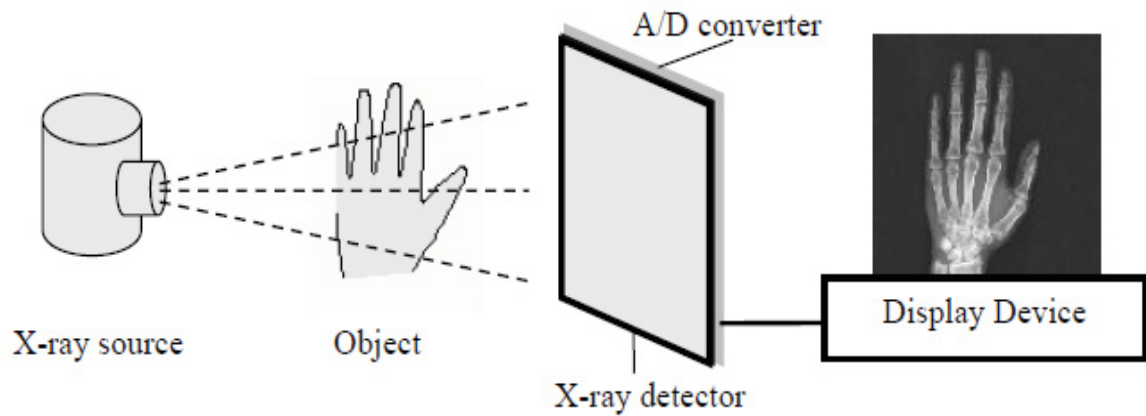


**Figure 1.1:** Schematics for digital radiography system [2].

The uniform X-ray passing through an object results in differential attenuation. As a result, the intensity of the radiation which reaches the detector is modulated. As shown in figure 1.1, the attenuation of X-rays is different in various parts of the human body (bone or soft tissue). The detectors detect these attenuated X-rays and give the results in grey shades on an X-ray image.

Only 35% of all X-ray diagnostic devices used in medical X-ray imaging are from the solid state, digital X-ray system. Most of the medical imaging is still performed by film based analog process [2]. The analog process starts with loading film into screen cassette for X-ray exposure and finally forwarding the cassette towards the dark room for

development so that the film is suitable for making a medical diagnosis. Although this is a very simple and cost effective process, this process takes a lot of time to complete. Real time imaging is also impossible in this process. A digital radiography can be an alternating solution for solving problems related with analog system.

### **1.3 X-ray image detectors**

Digital radiography (DR) overcomes nearly all of the disadvantages inherent in film based traditional radiography. In DR, X-rays are converted into electrical signals. This signal is then digitized for further processing. Also at the same time this process meets the requirements for real-time imaging. Images can be viewed on a computer screen, enabling computer aided diagnosis, and would allow the image to be transmitted via the communication link for immediate second opinions and stored electronically. Furthermore, reduced dose are required in DR system. This is an advantage in DR system as X-rays are ionizing radiation and can cause mutations in living cells with the increased dose.

#### **1.3.1 Flat panel detectors**

After an extensive research in 1990s, the large area thin-film transistor (TFT) or switching diode self-scanned active-matrix array (AMA) became technologically acceptable for xeroradiography. Xeroradiography is known as X-ray imaging system based on stabilized amorphous selenium (a-Se). When this active-matrix array is integrated with the flat panel detector concept then it is known as active-matrix flat-panel imagers or AMFPI.

In indirect conversion based FPXIs, a phosphor layer, such as gadolinium oxysulfide ( $Gd_2O_2S$ ) or a structured scintillating phosphor, such as cesium iodide (CsI) are used for absorption of incident X-rays. These layers are connected with AMA. There can be two kinds of scintillators: structured and unstructured. In case of unstructured one, the spreading of the visible light decreases the spiral resolution. On the other hand, structured scintillator helps to reduce the light spreading [3].

In direct conversion FPXIs, there is no intermediate ‘state’ from the incident X-ray to charge collection. A suitable photoconductor works as a converter to convert the absorbed X-ray photons directly to collectable charge carriers.

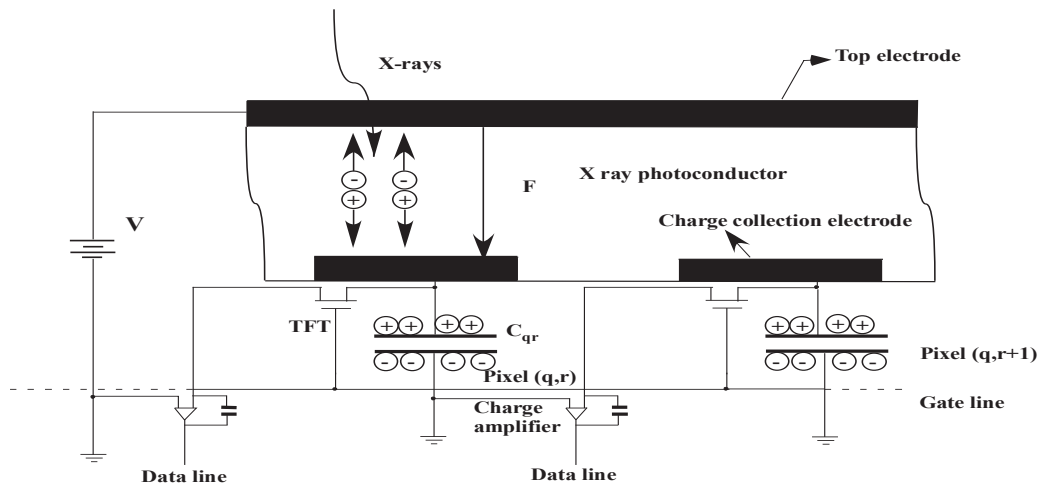


**Figure 1.2:** A simplified schematic diagram of the cross section of a single pixel with a TFT [2].

A simplified illustration of a direct conversion X-ray image detector is shown in figure 1.2. In a-Se based FPXI, the AMA is coated with X-ray photoconductive layer so that it

can work as a transducer for X-ray to charge collection. As shown in figure 1.2, the electrodes that receive the X-ray radiation is the top electrode (also known as radiation-receiving electrode) whereas the bottom electrode collects the charge hence known as charge collection electrode.

The top electrode may be positive or negatively biased. Electron hole pair (EHPs) are generated in the photoconductive layer due to the absorption of the X-ray photons. Number of electron and hole pairs generated in the photoconductor is proportional to the photon flux and the photon energy. For positive bias, electrons are collected at the top of the electrode and the photo generated charge in the photoconductor is collected on pixel capacitor,  $C_{qr}$  which allows the charge signal  $Q$  on  $C_{qr}$  to be read out into the external circuit that has a charge amplifier as indicated in figure. 1.2. The magnitude of the accumulated charge depends on the incident X-ray over the pixel.

## **1.4 Typical specification of digital X-ray system**

FPXI must be able to meet certain requirements in order to be used for different imaging tasks related to the clinical need of the particular image including mammography, chest radiography and fluoroscopy. Table 1.1 summarizes these requirements.

**Table 1.1** Parameters for digital X-ray imaging systems for different major applications.

The maximum energy of the emitted X-ray tube during the exposure is equal to the  $kV_p$  value (data taken from [3].) Here  $kV_p$  is peak kilo voltage which is the maximum voltage applied across the X-ray tube.

<b>Clinical Task</b>	<b>Chest Radiography</b>	<b>Mammography</b>	<b>Fluoroscopy</b>
<b>Detector size</b>	35 cm × 43 cm	18 cm × 24 cm	25 cm × 25 cm
<b>Pixel size</b>	200 μm × 200 μm	50 μm × 50 μm	250 μm × 250 μm
<b>Number of pixels</b>	1750 × 2150	3600 × 4800	1000 × 1000
<b>Readout time</b>	~ 1 s	~ 1 s	~1/30 s
<b>X-ray tube voltage</b>	120 kVp	30 kVp	70 kVp
<b>Average exposure</b>	300 μR	12 mR	1 μR
<b>Range of exposure</b>	30 – 3000 μR	0.6 – 240 mR	0.1 – 100 μR

## 1.5 Motivation

In presence of large applied field ( $10V/\mu m$ ), incident X-ray photons are converted directly to charge carriers in the a-Se layer and drifted towards the electrodes on either side of the layer in different X-ray imaging detectors. This field introduces the dark current to flow without the appearance of the incident radiation and eventually it becomes a source of noise which can reduce the dynamic range of the detector. It is considered that the main reasons of the high dark current is the injections of the carriers from the metal contacts rather than the bulk thermal generation current as the mobility gap for a-Se is very high (about  $\sim 2.2$  eV ) [4],[5]. Low level of dark current is observed in multilayer detectors with thin (a few microns) blocking layers sandwiched between metal contacts and bulk of the a-Se [6],[7]. These  $n$  and  $p$  type blocking layers used as an unipolar

conducting layer that allows the transport of the oppositely charged carriers but trap downs the holes and electrons respectively due to the high concentrations of deep trap centers available in these layers. As a result, just after the applied bias, electric field profile is changed as well as carrier injections from the metals are reduced. So this leads to the decay of the initial high dark current. However, the origin of this time dependency of the dark current decay is still a challenging question.

Frey *et al.* have studied on the transient behavior of the dark current [8]. They found evidence that dark current is dependent on the  $n$  layer thickness; it also decreases with the increasing thickness of  $n$ -layer. The dark current model of Mahmood *et al.* explains the transient behavior which reaches a steady state within a 1000s of the application of the bias. However, with a 208  $\mu\text{m}$  thick  $n$ - $i$ - $p$  detector, a steady state condition before the 1000s mark is not observed. Lack of distribution of deep hole traps and taking only two discrete deep hole traps are considered to be the reasons behind this transient decay. Also the trap distribution and the concentration of trap center in alkaline doped  $n$  type layer are still unknown. A systematic study of the density of these defect states can clarify the transient as well as the steady state behavior of the dark current. This can help out to reduce the magnitude of the dark current and hence the increase of the dynamic range of the detector. So the determination of the energy distributed defect density in the hole blocking layer of a-Se multilayer detector is the basis for the explanation of the transient behavior in the dark current.

Concept of impact ionization and its prospect on the avalanche multiplication leads the development in mammography, tomosynthesis, protein crystallography, and positron emission mammography technology where low dose expose are needed. a-Se is currently the only amorphous material to perform impact ionization at very high field (above  $\sim 70$ - $80$  V/ $\mu\text{m}$ ). High-gain Avalanche Rushing Photoconductor structure known as HARP is commercially available high gain a-Se device for an optical image sensor [9]. The detector consist of a indium tin oxide (ITO) glass with a  $\sim 10$ - $30$  nm cerium oxide ( $\text{CeO}_2$ ) as hole blocking layer on the front side as the light receiving side and thin layer of diantimony trisulfide ( $\text{Sb}_2\text{S}_3$ ) for electron blocking layer on the back side to receive electron beam [10]. The acceleration of electron hole pairs in a-Se layer depends upon applied field. However with the increase of electric field it pursues the dark current to increase.

A few potential detector structures for avalanche a-Se detectors are proposed in the literature [10]. The sources and mechanisms of dark current decay and their magnitude in these structures are not clearly understood. The detector structure must show a very low dark current and not accumulating X-ray generated carriers in the a-Se layer. A physics-based model considering various sources of dark current such as bulk thermal generation, carrier depletion, carrier injection and multiplication is essential for optimizing a-Se avalanche detector structure.

## 1.6 Research objective

The objectives of this research are defined in view of the present challenges (unknown density of defect state in hole blocking layer, dark current mechanism in a-Se avalanche detector under avalanche phenomena) in X-ray imaging detectors. The research tasks are as follows:

- Determination of Density of states near valance band of hole blocking layer of amorphous selenium multilayer X-ray detectors.
- Determination of optimum traps depth in  $n$  layer for faster dark current decay.
- Investigation of the physical mechanism for transient and steady state dark current in a-Se avalanche detectors.
- Determination of the multiplication factors for various current components in a-Se avalanche detectors.

In this thesis, the tasks are performed through theoretical modeling validated by the recent published experimental results.

## 1.7 Thesis outline

This dissertation combines with five chapters. In chapter 1, a brief understanding of the X-ray imaging and flat panel X-ray imaging detectors are discussed. Following on, the motivation of this research has also been described. The chapter concludes with the description of the research objectives and the outline of the thesis.

In Chapter 2, different conceptual theories and various terms of imaging detectors definition are described. These includes: X-ray photoconductor, the basic properties of a photoconductor, amorphous materials and density of states of a-Se; effects of stabilized a-Se in the X-ray detector. This chapter concludes with the brief observation on the a-Se avalanche detectors.

In Chapter 3, a theoretical model is developed for the determination of density of states near valance band of hole blocking layer of a-Se multilayer X-ray detectors. The developed model is validated with the measured and published experimental results with different alloyed multi-layer a-Se detector structures. At the end of this chapter, variation in the transient behavior of the dark current with different structures is observed.

In Chapter 4, various effects of different structures for a-Se avalanche detectors is discussed. A physics-based quantitative model for the transient and steady state dark current mechanisms in different a-Se avalanche detectors is developed. This developed model is validated with the measured experimental results on various structures. The chapter concludes with a brief discussion for the optimized a-Se avalanche detector structure for a low dark current.

Chapter 5 concludes this thesis and gives some recommendations for future works.

## CHAPTER 2

### Background and Concepts

In this chapter, necessary background concepts such as X-ray photoconductor and important features for ideal photoconductor are discussed. Density of state for amorphous materials, effect of alloyed a-Se and finally the concept of amorphous avalanche multiplication are the main points in this chapter.

#### 2.1 X ray photoconductor

Superior image quality and simple structure make the direct conversion flat panel X-ray image detector suitable for high resolution imaging such as *mammography*. The key property of such an improved performance critically depends upon the selection and design of X-ray photoconductor.

##### 2.1.1 Ideal photoconductor

There are many criteria that make an X-ray photoconductor nearly perfect. A few important photoconductor properties related to dark current are discussed below.

- a) Flow of current in absence of any irradiation must be as low as possible in X-ray imaging detectors. This current, known as dark current, is a source of additive noise towards the signal. It reduces the dynamic range as unnecessary charges are accumulated on the pixel capacitor [4]. For this reason, the sources of dark current

should be limited. Therefore charge injection from the contacts should be minimal at the very high applied field. High potential barrier and low electric field can ensure low injection of current. Thermal generation of injected carriers in the bulk of the photoconductor should also be negligibly small by making the dark conductivity practically zero. The dark current should be as small as possible (preferably smaller than  $100 \text{ pA/cm}^2$ ) for diagnostic X-ray imaging applications [11].

- b) The band gap for the photoconductors should be optimized. Photoconductors need high intrinsic X-ray sensitivity for which amounts of radiation energy needed to create an electron hole pair (EHPs) should be small. This energy, denoted as  $W_{\pm}$  for many photoconductor, is proportional to the band gap  $E_g$  [12]. On the hand, for low dark current the dark conductivity should be small. So band gap should be optimized to fulfill the criteria for photoconductor.
- c) The schubweg can be defined as distance travel by the carrier before it is in the deep trap situation and unrecoverable. Schubweg must be greater than the photoconductor thickness for both electron and holes. Ideally,  $\mu\tau F \gg L$  where,  $\mu\tau F$  is the schubweg and  $L$  is the thickness for the photoconductor. Then the loss of generated EHP due to deep traps is negligible.

### **2.1.2 Different photoconductors**

The photoconductor like a transducer converts photon energy to electrical charge. Only amorphous or polycrystalline photoconductors are currently suitable for large area direct

conversion X-ray image detectors. In this chapter, the various properties of amorphous materials as a photoconductor are discussed.

## **2.2 Amorphous materials**

Considering the periodicity in their atomic structure solid are broadly categorized into three groups; *crystalline*, *amorphous* and *polycrystalline*. In crystalline materials atoms are arranged in an orderly manner. Each and every nearest neighbor atom maintains an identical number of bonds among them. Also inter-atomic spacing along with the bond length and bond angle are well established in the crystalline materials. This periodic and rigid geometry is observed throughout the material. On the other hand, amorphous materials are the ones in which the component atoms lack such a periodicity with a long range disorder and has a periodicity for few atomic distances.

Amorphous as well as crystalline materials can be prepared for the materials that are used in large area applications such as displays, solar cells, X-ray detector, and also for other similar large area applications. In this case, amorphous materials have an added advantage because the growth of such materials does not require the controlled growth like their crystalline counterparts.

The main advantageous point for the a-Se in the field of direct conversion flat panel X-ray detector is that they can be easily prepared as thick films or layers over large areas by thermal evaporation in a conventional vacuum coater [13]. As the melting point for

selenium is 220°C, with a competitively low ‘boat’ temperature, vitreous selenium pellets are melted into it.

### **2.2.1 Band structures of amorphous semiconductor**

N. F. Mott in 1967 was the first to generalize the band theory of crystalline semiconductors to amorphous materials. He postulated shorter range order amplitude of Bloch wave functions in the amorphous semiconductors [14]. This leads to the conversion of sharp band edges in periodic crystalline solid to the ‘tails’ of localized states in amorphous materials. Abrupt change in mobility in the localized state makes a ‘mobility gap’ similar to the band gap of crystalline semiconductor.

Marshall and Owen [15] performed studies on the charge transport properties of amorphous chalcogenide semiconductors. They introduced the defect state perception as the presence of localized states in the mobility gap in addition to the tail states. They proposed that well defined defects in the amorphous structure such as dangling bonds, chain ends, vacancies, substitutional impurities, interstitials etc are the consequence of localized mid-gap states. Figure 2.1 shows the different proposed models for density of states.

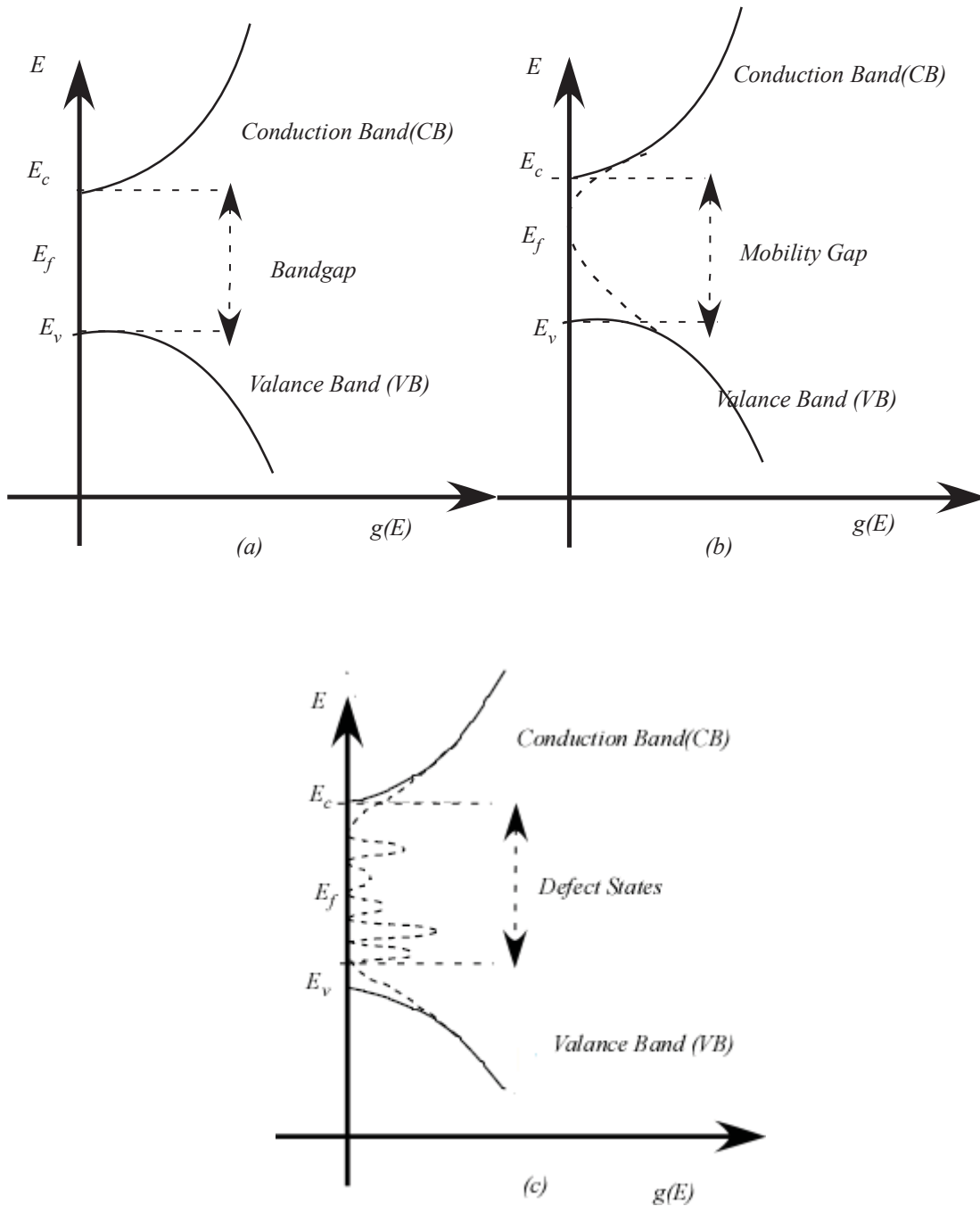


**Figure 2.1:** Various proposed models for density of states  $g(E)$  as a function of energy. (a) DOS model for crystalline semiconductors (b) Mott's model (c) Marshall and Owen model.

### 2.2.2 Density of states model for amorphous selenium

Selenium is a member of group VI of the periodic table. The set of elements which are located in that group are called chalcogens. The electronic and carrier transport properties of amorphous structure are well connected with the DOS distribution within the mobility gap. Two proposed DOS models for a-Se will be discussed in this section.

The most commonly accepted model for DOS of a-Se is proposed by Abkowitz in 1988 [16]. This model was based on a number of published experimental results. It is an extension of Owen-Marshall model.

This model can be seen in figure 2.2 and the features are highlighted bellow:

- The mobility gap is effectively 2.22eV.
- The electron and hole shallow traps are located  $\sim 0.35$  eV below the conduction band ( $E_C$ ) and  $\sim 0.28$  eV above the valence band ( $E_V$ ), respectively.

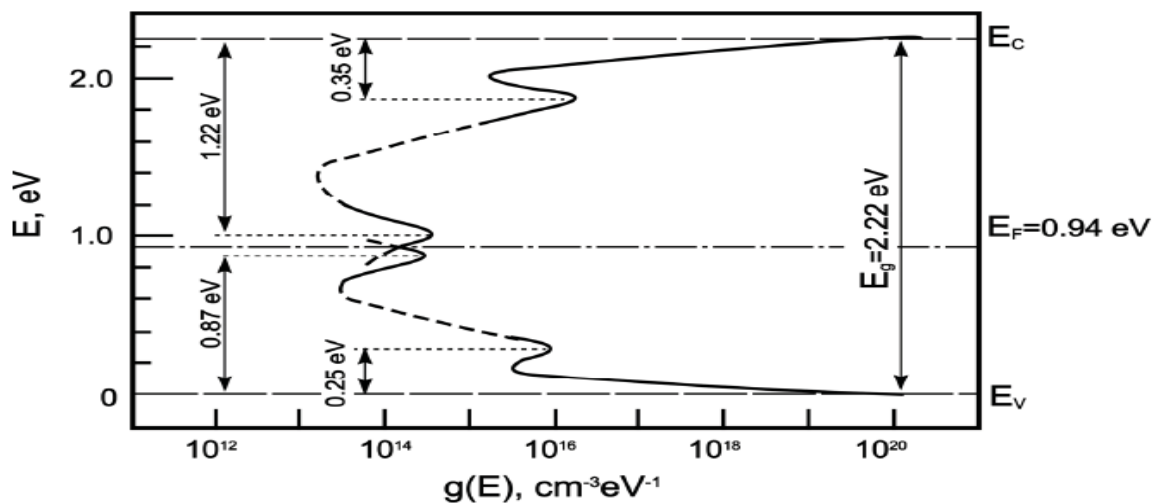


**Figure 2.2:** The density of electronic states in a-Se as proposed by Abkowitz [16].

The localized states near the Fermi level are called deep traps. Shallow traps are the localized states near the band edges.

The level of carriers being ‘deeply’ trapped in a-Se depends on how the materials are alloyed or doped. In case of X-ray imaging applications, deep defect states are of particular interest. Carrier lifetime or trapping time duration is dominated by deep states. In shallow traps, due to the presence of disorder induced localized states, the microscopic mobility  $\mu_0$  is modulated by trapping centers near the band edges in a-Se. Shallow traps decreases carrier mobility and thus effective drift mobility of the carriers’ changes. These traps are characterized by their capture and release time. The capture time is the average untrapped time for the carrier to have motion in the extended state where they have finite band transport mobility before being shallow trapped. On the other hand, release time is the mean time spent by the carrier in the trap before released towards the conduction band. So the effective drift mobility is increased with a transport parameter  $\theta$  [17]

$$\mu = \theta\mu_0 \quad (2.1)$$

Here,  $\theta = \frac{\tau_r}{\tau_r + \tau_c}$  where  $\tau_r$  is the release time and  $\tau_c$  is the capture time. In this trap-

limited transport system, the characteristic time is  $\tau_c = \frac{1}{C_t N_{td}}$  and the carrier release

time is,  $\tau_r = \omega_0^{-1} \exp(E_t / kT)$ .

where  $k$  is the Boltzmann constant,  $T$  is the absolute temperature,  $\omega_0$  is the attempt-to-escape frequency,  $E_t$  is the depth of the trap,  $N_{td}$  is the density of traps and  $C_t$  is the capture coefficient which depends on the types of the traps.

Recent attempts of Koughia using comparison between time of flight (TOF) measured photocurrents of electrons and holes with previous theoretically calculated photocurrent, observed an exponential tail state near valance bands as shown in figure 2.3 [18],[19],[20]. The main features of their observation are:

- There are peaks at 0.3 eV and at 0.45-0.5 eV below  $E_c$ .
- A featureless, monotonically decreasing distribution almost like an ‘exponential tail’ in energy up to  $E_v + 0.4$  eV, without the 0.28 eV peak near the valence band as in Abkowitz model which was thought to control the hole drift mobility.

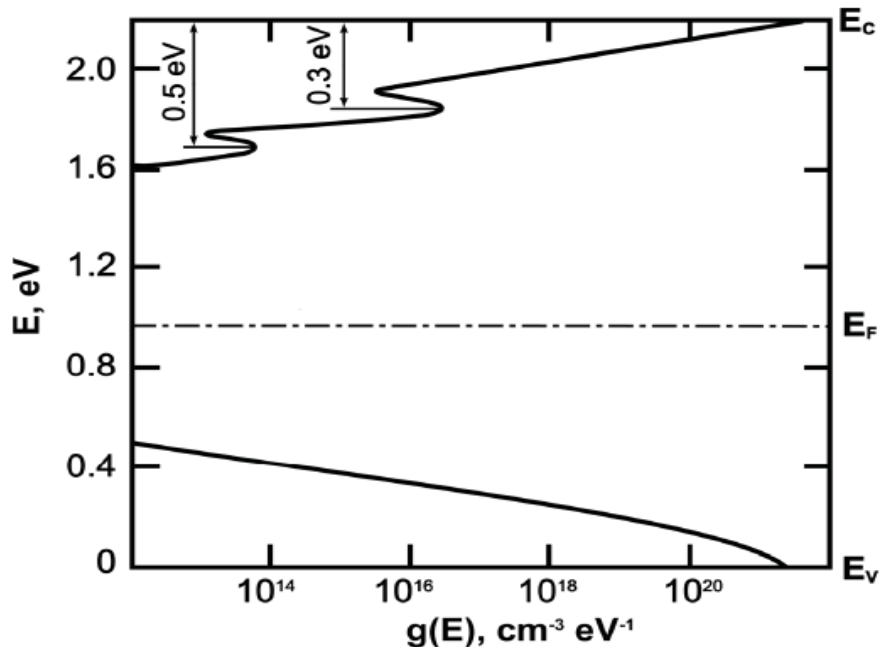


**Figure 2.3:** The density of electronic states in a-Se as proposed by Koughia [18][19][20].

The DOS model by Abkowitz is supported by other experimental evidence. This model has shown sharply (exponentially) decaying shallow trap densities from the transport bands. On the other hand, Koughia proposed model results were supported by Monte

Carlo simulations which simulated the photocurrent for the DOS [20]. Abkowitz model is considered to be the promising one for intrinsic a-Se.

### 2.3 Amorphous selenium as an X-ray photoconductor

Intrinsic a-Se has a tendency to crystallize over the time. a-Se can doped with small amount (0.2-0.5%) of Arsenic (As) and 0-40 ppm (parts per million) of Chlorine (Cl). Different properties of ‘stabilized a-Se’ are listed in table 2.1.

**Table 2.1.** Properties of stabilized a-Se (a-Se: 0.2-0.5% As +10-40 ppm Cl) films at room temperature (data taken from ref [13])

Properties	Typical Range	Schubweg at $5V\mu\text{m}^{-1}$	Comment
Hole mobility $\mu_h$	$\sim 0.12\text{cm}^2/\text{V-s}$		Well reproducible, Probably shallow trap controlled.
Electron mobility $\mu_e$	0.003-0.006 $\text{cm}^2/\text{V-s}$		Decreases rapidly with As addition. Probably shallow trap controlled.
Hole lifetime $\tau_h$	20-200 $\mu\text{s}$	1.2-12 mm	Depends on the substrate temperature.
Electron lifetime $\tau_e$	200-1000 $\mu\text{s}$	0.3-1.5 mm	Sensitive to small quantity of impurities.
Hole range $\mu_h\tau_h$	$2-20\times 10^{-6}\text{cm}^2/\text{V}$		Substantially higher than lead(II) iodide ( $\text{PbI}_2$ )
Electron range $\mu_e\tau_e$	$1-6\times 10^{-6}\text{cm}^2/\text{V}$		Somewhat higher than $\text{PbI}_2$

### **2.3.1 As effect**

Arsenic (As) atoms are triply bonded. This leads to improve the stability of the composite film and helps to prevent crystallization. Works on the transport properties of alloyed a-Se films confirmed that the addition of As reduces the hole lifetime but does not change the hole mobility [21]. Conversely, the addition of As increases the lifetime of electrons. As a result, the electron range ( $\mu_e\tau_e$ ) increases which is admirable for the for X-ray photoconductors where the bottom electrode is connected to negative terminal. This makes the overall concentration of deep trapping reduced.

### **2.3.2 Cl effect**

Typical influences of Chlorine (Cl) on electron and hole transport in pure Se films is observed in literature [22]. Small amounts of Cl have almost no effect on the carrier mobility-lifetime product. However, the introduction of Cl has a drastic effect on the electron lifetime. On the other hand, 20 ppm of Cl can increase the hole lifetime as well as compensate the effects of 0.2% As. Also this amount of Cl can strongly increase the hole mobility-lifetime product.

## **2.4 Practical a-Se multilayer detector**

With the use of doped a-Se as a blocking layer, the dark current in a-Se based X-ray images can be reduced. Multilayer a-Se based detectors are now used for X-ray imaging sensors. The multilayer a-Se based detectors can be *n-i-p* or *p-i-n* type depending on the

type of collected charge by the pixel (bottom) electrode. The first letter in the multilayer structure notation refers to the layer next to the X-ray receiving electrode.

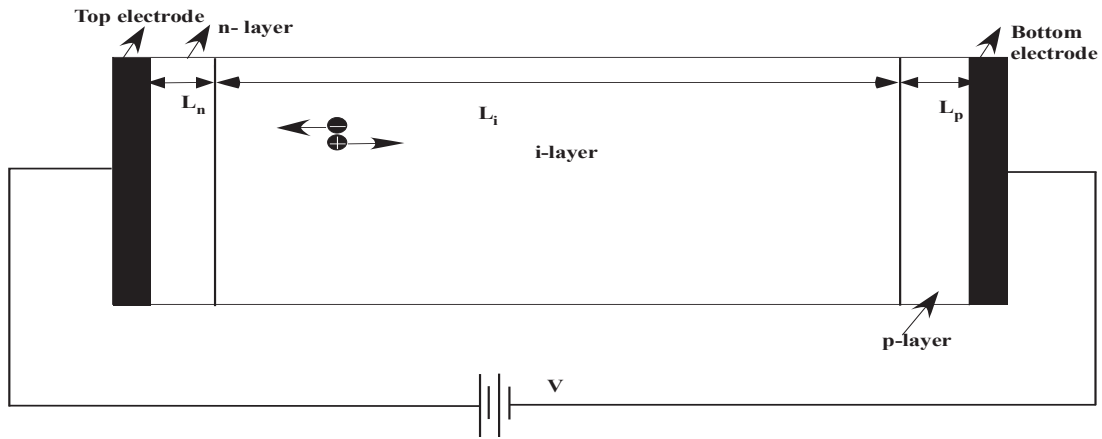


**Figure 2.4:** A multilayer a-Se structure.

A multilayer a-Se based detector structure is shown in figure 2.4. The  $p$  and  $n$  layers are usually thin compared with  $i$ -layer. Here the structure is fabricated in such a way that  $n$  layer is appropriately doped to trap holes making the hole life time ideally zero and allow the electron to transport. Similarly, the  $p$  layer is also doped appropriately so that it can trap electrons allowing the hole to transport. This signifies that the  $p$  and  $n$  layers have a very high concentration of deep trap centers for electrons and holes respectively. The thickness of these blocking layers are few  $\mu\text{m}$  (usually 4 to 8  $\mu\text{m}$ ) whereas the total photoconductor thickness is about  $100\mu\text{m}$ .

The conventional definition of the  $n$  and  $p$  layer is different in a-Se structure and it is based on mobility lifetime product  $\mu\tau$  where  $\mu$  is the drift mobility and  $\tau$  is deep trapping time or lifetime. However the Fermi levels do not locate necessarily in these layers. In

case of a-Se *n*-type layer, the condition is  $\mu_e \tau_e \gg \mu_h \tau_h$ , where the subscripts *e* and *h* represents electrons and holes, respectively. Depending upon the type of collected charge by the bottom electrode or pixel electrode, the multilayer a-Se detector can be *n-i-p*, *p-i-n* or *n-i* type. In all cases this structure is reverse biased. In *n-i-p* structure top electrode is positively biased and X-ray generated holes are collected at the bottom electrode.

## 2.5 Amorphous selenium avalanche detector

During 1980s concept of impact ionization which leads to avalanche multiplication was explained in a-Se. It was an interesting result to observe avalanche multiplication on amorphous selenium as amorphous semiconductors have low carrier drift mobility because of the random potential fluctuations in their structures. Holes in a-Se gain enough energy from the high electric field to perform impact ionization and hence leads to secondary charge creation.

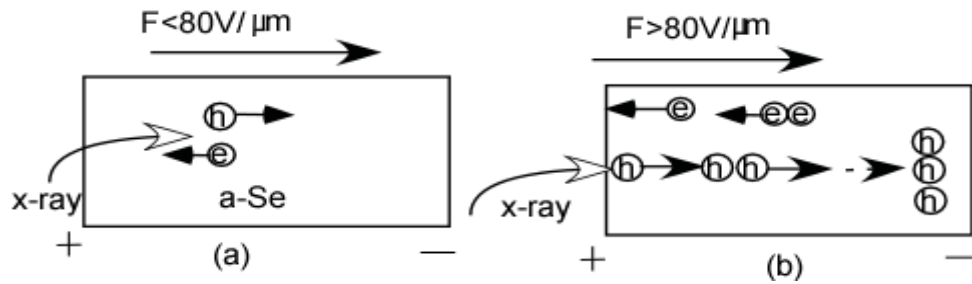


**Figure 2.5:** Process of avalanche multiplication (a) under non avalanche field (b) under avalanche field with more electron-hole pair due to impact ionization [23].

Figure 2.5 shows how high electric field effects on hole impact ionization in a-Se which initiated avalanche in a-Se. At electric fields which exceeds a certain avalanche

multiplication threshold  $F_{th}$ , holes gain enough kinetic energy to create additional EHPs along their paths towards the pixel electrodes. A useful avalanche gain of 1000 has been observed for a  $\sim 30\mu\text{m}$  thick a-Se with a field of  $92\text{ V }\mu\text{m}^{-1}$  [24]. This observation leads to improve signal to noise ratio of the a-Se imaging detector suitable for low dose X-ray imaging.

The concept of avalanche gain in a-Se has been used in HARP. This structure contains a thin layer of  $\text{CeO}_2$  on the front side ( $\sim 20\text{nm}$ ) of a-Se layer and  $\text{Sb}_2\text{S}_3$  layer at back side.  $\text{CeO}_2$  works as blocking layer to prevent the injection of holes from the anode, as it is slightly  $n$  type and has a wide band gap. On the other hand,  $\text{Sb}_2\text{S}_3$  contains a large number of deep electron traps making a negative space charge barrier when all the traps are filled. As a result, this blocking layer prevents electron from the bottom electrode. The avalanche a-Se detectors are being proposed in all solid state device based X-ray image sensors by replacing the electron beam to a pixilated detector structure.

For avalanche formation the applied field has to be above  $\sim 70\text{V}/\mu\text{m}$  range [23]. Hole injection from the positive electrode has been a dominant reason for the development of the dark current. So, hole blocking mechanism is an important parameter in case of dark current. A proper hole blocking layer should have the following aspects

- The potential barriers for hole contacts should be high enough between the metal electrode and the a-Se layer.
- There should be enough hole trapping layers with a low hole mobility.
- Electrons should be able to move freely in the uni-conducting layer.

Above all, the layer should have the compatibility for large area electronics semiconductor fabrication process.

In this thesis, three potential avalanche selenium detector structures for the flat panel digital X-ray imaging are considered. Figure 2.6 shows the basic structure of these three devices.

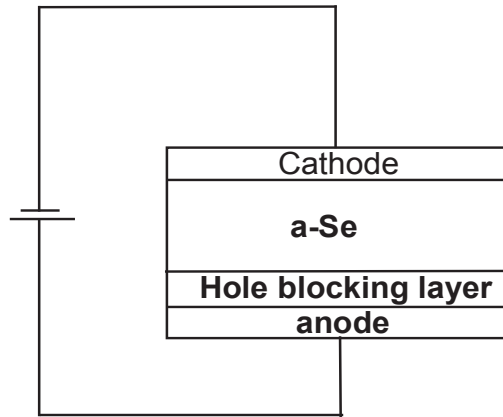


**Figure 2.6:** Schematic structure for observation of hole blocking mechanism

Different materials are used as a hole blocking layer and carrier transport in both modified (with different hole blocking layer) and original HARP is observed.

Another aspect of avalanche a-Se photoconductor is in measuring the diffraction patterns where sensitive detectors and large dynamic range is needed. In protein crystallography, avalanche a-Se detectors are used for their high sensitivity for each incident X-rays due to avalanche nature [25].

## **2.5 Summary**

In this chapter, background concepts related to the X-ray detector are discussed. X-ray photoconductor, important features for ideal photoconductor, DOS in a-Se, and finally commercial a-Se and a simple avalanche a-Se detector structure are described in this chapter.

## CHAPTER 3

### Density of defect states of $n$ layer of $a$ -Se multilayer X-ray detectors

Dark current is a source of noise and it also reduces dynamic range of the detector. It is one of the most important factors for the selection of the photoconductor for X-ray imaging applications [26]. Under normal operating bias (that creates an applied electric field of  $\sim 10$  V/ $\mu\text{m}$ ) the dark current in a simple metal/ $a$ -Se/metal structure is particularly high ( $\sim 1$ – $100$  nA/cm<sup>2</sup>) which is unacceptable for X-ray imaging application [27]. Recent experiments on  $a$ -Se detectors have shown that low dark current can be achieved in a multilayer detector where thin blocking layers are used between the intrinsic layer ( $i$ -layer) of  $a$ -Se and the metal contacts [27]. The blocking layers are  $p$ -type and  $n$ -type layers which are appropriately doped to serve as unipolar conducting layers that can easily trap electrons and holes, respectively, but allow the transport of oppositely charged carriers. The carrier transport properties and energy distributed defect densities in these blocking layers are totally unknown. The previous theoretical dark current model has been validated with the measured and published experimental results for different  $a$ -Se detectors structures with the shape of transient dark current by considering Schottky emission of holes from the positive contact and carrier trapping in two discrete deep trapping states in the  $n$ -layer [5]. In this chapter an extended version of that transient dark current model by incorporating energy distributed deep trapping states has been

developed. The field dependent barrier height is also explained by the thermally assisted tunneling process. The model is compared with the experimental transient dark current results on commercial *n-i-p* and cold deposited *n-i* a-Se detector structures and determines the energy distributed deep defect densities in these two types of n-layers.

### 3.1. Sources of dark current

The main contribution for dark current could be from three potential sources: initial carrier depletion from the bulk, bulk thermal generation and carrier injections from the metal contact. Generation of charged carriers from the localized states within the mobility gap could leads to the flow of dark current, which are commonly known as thermal generation current. Charge carrier depletion right after applying the bias constitutes transient current.

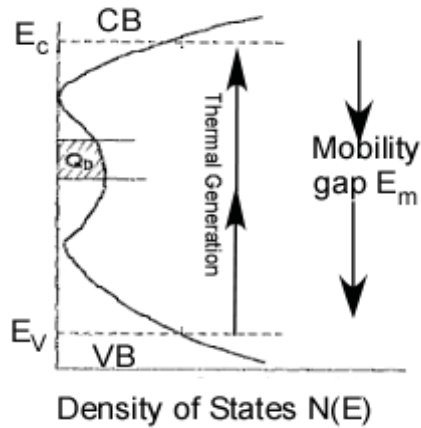


**Figure 3.1:** Origin of thermal generation current from the band diagram. The shaded area represents depletion of charge [28].

The figure 3.1 shows the origin of bulk thermal generation from the midgap defect states within the mobility gap. Considering the Poole-Frenkel effect where the potential barrier of the trapped carrier is reduced, the generation rate of the holes within the  $kT$  of the Fermi level [29] is

$$g = N(E_f)\omega_0 \exp\left(-\frac{E_f - E_v - \beta_{pf}\sqrt{F}}{kT}\right) \quad (3.1)$$

where  $N(E_f)$  is the density of the localized states at energy  $E_f$  near the midgap,

$\beta_{pf} = \sqrt{\frac{e^3}{\pi\epsilon_s}}$  is the Poole-Frenkel coefficient and  $F$  is the applied electric field.

Assuming that holes are fully depleted and total generation of holes are collected then the thermal generation current density would be [28]

$$J_{th} = egL = eN(E)\omega_0 \exp\left(-\frac{E_f - E_v - \beta_{pf}\sqrt{F}}{kT}\right)L \quad (3.2)$$

Here  $L$  is the thickness of the photoconductor.

Carrier injection at the metal/a-Se contact depends on the contact field and metal, and hence on the metal-semiconductor barrier height. For low mobility ( $\mu < 1\text{cm}^2/\text{V-s}$ ) semiconductor such as a-Se, the current transport is controlled by its mobility.

## 3.2 Dark current in a-Se films

During 1960s and 1970s several works were reported focused on the dark current measurement in metal/a-Se/ metal sandwich structures. At that time no general conclusion has been reached for the origin of steady-state dark I-V characteristics of these structures. Some of the researchers agreed that the dark current in Au/a-Se/Cu

structures is due to the effects of Pool- Frenkel or Schottky emission from the electrode. Johanson *et al.* postulated that the dominant source of the dark current is the hole injection from the positive contact in the metal/intrinsic a-Se/ITO (indium tin oxide) and it decays with time in a non-exponential manner immediately after the application of a bias voltage [30].

Fabricating a thin effective unipolar conducting layer(blocking layer) at the contact is a reliable method to reduce dark current in a-Se detectors below the acceptable level ( $<100 \text{ pA/cm}^{-2}$ ) . In this process, injected charges from the metal contacts are trapped in the blocking layer and allow transporting the oppositely charged carriers [2]. Hence the subsequent charge injection from the metal into a-Se is minimized. The blocking layers have been achieved through the use of a thin *n* layer of alkali metal doped a-Se and a thin *p* layer of a-As<sub>2</sub>Se<sub>3</sub> to trap holes and electrons from the injected positive and negative contacts respectively [30]. Recent work has shown that an *n-i* structure with cold deposited *n*-layer can also show very low dark current [27].

Theoretical work, which is extended in this thesis, by Mahmood *et al.* [5] have shown good agreement with experimental results of measured dark current transient in the *n-i-p* structured a-Se samples. Their work is operated on the principle that the dark current transient is controlled entirely by the injection of carries from the positive contact over a Schottky barrier and carrier trapping in two discrete deep trapping states in the *n* layer. As a result, uniform conducting layers can build up a space charge near the contact and reduces the electric field. This makes the dark current drop down with time until it

reaches the steady state where the rate of trapping and release of carriers reaches equilibrium. It is also been found that the effective barrier height for Schottky emission slightly decreases with the field [4]. In this chapter the transient model of Mahmood *et al.* has extended considering the field-dependent barrier height due to thermally assisted tunneling process and energy distributed deep trapping states. Also the model is compared with recently published experimental results of transient dark currents on commercial *n-i-p* and cold deposited *n-i* a-Se detector structures and determines the energy distributed deep defect densities (density of states, DOS) in these two types of *n*-layers. For having a low dark current and faster transient time to reach a plateau, a sufficient amount of trap densities with optimum trap energy depth is required. A physics based analysis is done in this chapter to determine the optimum trap depth in the *n*-layer for an efficient hole blocking layer.

### 3.3 The model

In a-Se based multilayer detectors, the top contact (radiation-receiving electrode) is generally blocking in nature, and the hole injection in *n-i-p* structure is mainly controlled by the Schottky emission process [5]. A Schematic diagram of a multilayer a-Se based X-ray image detector is shown in figure 3.2 (a). The injected carrier from the top contact to the semiconductor depends upon the electric field  $F_1$  at the interface. Figure 3.2 (b) shows the steady state electric field profile before applying any radiation in a-Se based *n-i-p* structures. The decrement of electric field at the metal contacts is due to the trapped carriers. High initial current and high carrier trapping in the blocking layers reduces the

uniformity of the electric field [5]. According to reference [8], the injected current density due to hole injection in the a-Se *n-i-p* structure is,

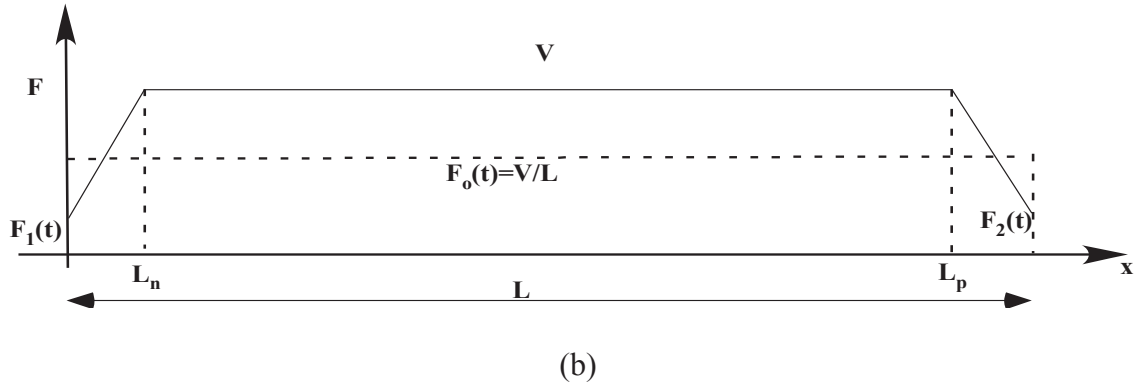
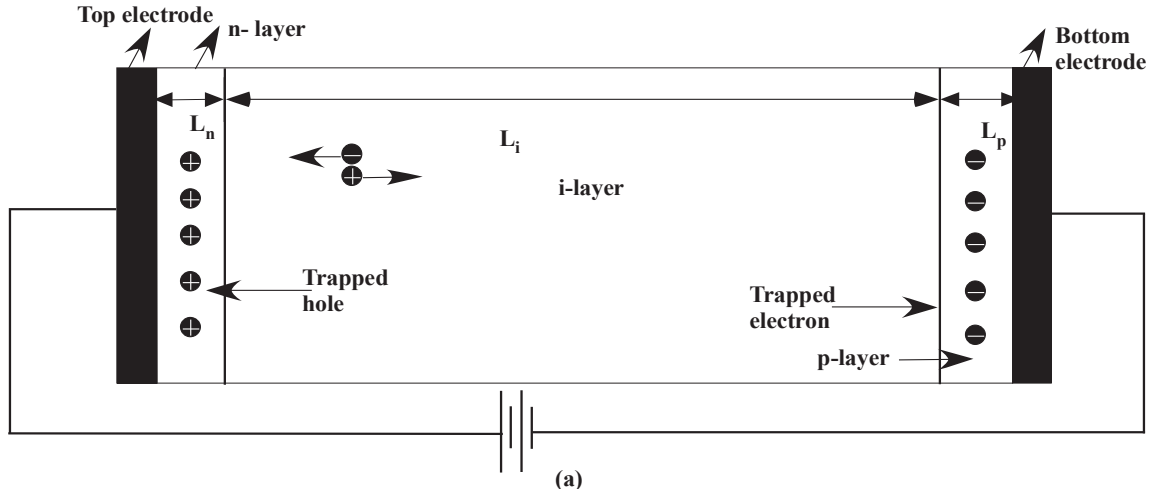


**Figure 3.2** (a) Schematic diagram of a multilayer a-Se based X-ray image detector. The electron-hole pairs are generated and then follow the electric field. (b) The relative magnitude of the field across the photoconductor is illustrated by  $F_0$  [31].

$$J_h(t) = e\mu_h N_V F_1(t) \exp\left\{-\frac{\phi_h(F_1)}{kT}\right\} \quad (3.3)$$

where  $e$  is the elementary charge,  $F_1(t)$  is the instantaneous electric field at the top electrode/ $n$ -layer interface,  $\mu_h$  is the effective hole mobility,  $T$  is the absolute temperature,  $k$  is the Boltzmann constant,  $N_V$  is the effective density of states in the valence band, and  $\phi_h$  is the effective barrier height for injecting holes from the top electrode into the  $n$ -layer. The resulting effective barrier height depends on  $F_1(t)$  by ,

$$\phi_h(F_1) = \phi_0 - \varphi_b - \varphi_t, \quad (3.4)$$

The quantity  $\varphi_0$  can be treated as an adjustable parameter, which is controlled by the interface conditions. Here, the term  $\varphi_b$  can be considered as the barrier lowering due to image force. This can be shown as

$$\varphi_b = \beta_s \sqrt{F_1(t)} \quad (3.5)$$

Where  $\beta_s = \sqrt{\frac{e^3}{4\pi\epsilon_{se}}}$  is the Schottky coefficient,  $\epsilon_{se} = \epsilon_0\epsilon_r$  is the permittivity of the photoconductor. And the term  $\varphi_t$  is considered as the barrier lowering due to the thermally assisted tunneling shown as

$$\varphi_t = \alpha F_1(t) \quad (3.6)$$

where  $\alpha$  is the effective tunneling distance, which is usually less than 2nm [32]. The quantity  $\alpha$  is treated as a free parameter.

The injected concentration for holes from the top contacts over a Schottky barrier can be modeled as

$$p(t) = N_V \exp\left\{-\frac{\phi_h(F_1)}{kT}\right\} \quad (3.7)$$

Once the carriers are injected into the a-Se layer, they move by drift mechanism. Diffusion component of current is negligible compared to its drift component because of very high applied voltage [5]. That is,  $J_h(t) = e\mu_h p(t)F_1(t)$  in the a-Se layer. The instantaneous electric field  $F_1(t)$  changes due to trapping/detrapping of injected holes in the energy distributed deep trapping states of the  $n$ -layer. The energy distributed deep trapping states are discretized in  $m$  number of segments/levels. The trapping rate equation for trapped holes at a trap level  $E_{tm}$  is [5],

$$\frac{dp_{tm}}{dt} = C_{tm}N_{tm}\theta_h \left[ 1 - \frac{p_{tm}}{N_{tm}} \right] p(t) - \frac{p_{tm}}{\tau_{rm}} \quad (3.8)$$

which encompasses trapping, the trap filling effect and trap release. Here  $N_{tm}$  is the initial unoccupied trap density at the trap level  $m$ ,  $C_{tm}$  is the deep trapping capture coefficients,  $p_{tm}$  is the trapped hole densities at the trap level  $m$ ,  $\theta_h = \mu_h/\mu_{0h}$ , and  $\mu_{0h}$  is the hole mobility in the extended states of a-Se layers, and  $\tau_{rm}$  is the release time constant for the deeply trapped holes. The release time  $\tau_{rm}$  is related to the trap depth  $E_{tm}$  from the mobility edge of the valance band by  $\omega_0^{-1} \exp(E_{tm}/kT)$ , where  $\omega_0$  is the attempt-to-escape frequency [5]. The attempt-to-escape frequency can be defined as the product of the maximum lattice frequency and a factor, equal to or less than 1, describing the probability of the hole(electron) entering the valance(conduction) band after receiving sufficient energy. The relation between  $\omega_0$  and  $C_{tm}$  can be determined by the principle of detailed balance, which gives  $\omega_0 = N_v C_{tm}$ .

It is assumed that during the applied field the electric field profile distribution across the structure will be uniform and as injected holes are trapped in the hole blocking layers and

subsequently released, the distribution of the space charge density also changes in the sample. As a result the electric field profile varies. This process is calculated by solving the Poisson's equation

$$\frac{dF(x)}{dx} = \frac{\rho(x)}{\epsilon_0 \epsilon_r} \quad (3.9)$$

with boundary condition

$$\int_0^L F(x) dx = V \quad (3.10)$$

Here,  $\rho$  is the charge density due to the trapped carriers,  $L$  is the thickness of the sample, and  $V$  is the applied voltage. Assuming uniform trapping in the  $n$  and  $p$  layer and negligible trapping in the  $i$ -layer the instantaneous electric field  $F_1(t)$  is determined by solving the Poisson's and energy distribution trapping rate equations in the  $n$ -layer is given by,

$$F_1(t) \approx F_0 - \frac{e}{\epsilon} \left( L_n - \frac{L_n^2}{2L} \right) p_t(t), \quad (3.11)$$

where  $F_0 = V/L$ ,  $V$  is the applied bias voltage,  $L$  is the total photoconductor layer thickness,  $L_n$  is the  $n$ -layer thickness,  $p_t(t)$  is the instantaneous trapped hole concentration in the  $n$ -layer. It is assumed in equation (3.7) that the  $p$ -layer thickness  $L_p \ll L$  for the  $n$ - $i$ - $p$  structure.  $p_t$  can be equated by ,

$$p_t(t) = \sum_m p_{tm}(t) \quad (3.12)$$

Here instantaneous trapped hole concentration in  $n$  layer can be discretize in to trapped hole densities with  $m$  number of trap levels.

### 3.4 Results and Discussion

The coupled algebraic-differential equations (3.3)-(3.12) are simultaneously solved using MATLAB to get the instantaneous electric field profile, trapped carriers, and dark current. The effective mobility of hole  $\mu_h = 0.12 \text{ cm}^2/\text{V}\cdot\text{s}$ , the ratio of band to effective mobility,  $\theta_h = 0.4$ , effective tunneling distance  $\alpha = 2 \text{ nm}$ , and  $\varepsilon_r = 6.7$  are taken in all calculations [26], [33]. The band gap,  $E_g = 2.2 \text{ eV}$ , and  $N_V = 10^{19} /\text{cm}^3$  are assumed in all layers [16], [34]. The developed model with the above parameters is verified with the measured and the published data to determine the density of defect states. Unless otherwise specified all the parameters mentioned above are fixed for all the theoretical calculations in this thesis. Other parameters such as effective barrier height ( $\phi$ ), trap center concentration ( $N_t$ ) and trap depth in the  $n$ -layer depend on the fabrication processes and therefore, these are considered as fitting parameters in the model.

#### 3.4.1 The dark current in $n$ - $i$ - $p$ structure:

The proposed model is applied on recently published experimental  $n$ - $i$ - $p$  structures [8]. The  $n$ -layer is  $6 \mu\text{m}$  thick and the overall thickness of the a-Se layer is  $\sim 208 \mu\text{m}$  [8]. With a distributed deep hole traps states, spread in energy, a modified trap rate equation (3.8) is

coupled with the other equations to match the transient results. Also by analyzing the transient behavior the density of defect state of alkaline doped n-layer is calculated.

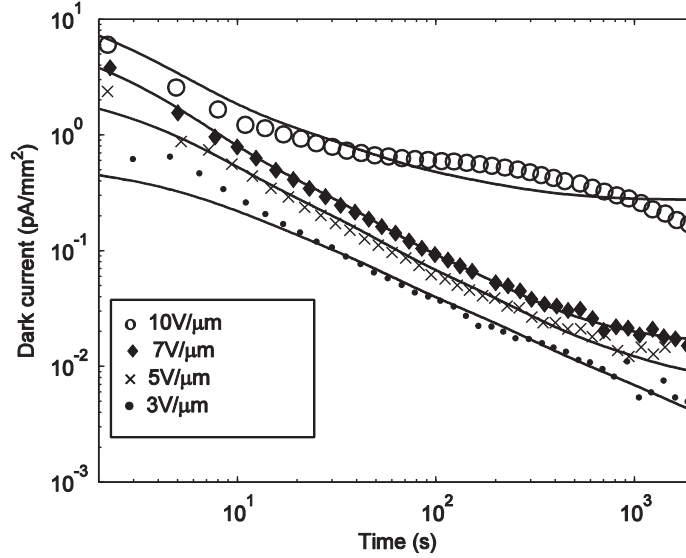


**Figure 3.3:** Dark current density of a-Se  $n-i-p$  sample as a function of time for four different positive applied fields. The symbols represent experimental data [8] and the solid lines represent the theoretical fit to the experimental data.

Figure 3.3 shows the dark current density as a function of time for four different applied fields  $F_0$  for an  $n-i-p$  detector structure (Analogic sample) [8]. The symbols represent experimental data and the solid lines represent the theoretical fit to the experimental data. The experimental data have been extracted from figure 7 of reference [8]. This model is compared with recently published experimental results on  $n-i-p$  a-Se detector structures and used to determine the energy distributed deep defect densities in the  $n$ -layer. For hole blocking  $n$  layer six discrete deep defect states,  $E_{tm} = 0.7, 0.74, 0.78, 0.82, 0.86$  and  $0.9$  eV is considered and the energy width of each state is  $0.04$  eV. As the thermal release time is very short for carriers in shallower trap levels ( $<0.7$  eV) hence these levels retain

very negligible trapped carriers. The validated parameters are  $\omega_0 = 5 \times 10^{11}$  /s with capture coefficient  $C_t = 5 \times 10^{-8}$  cm<sup>3</sup>/s, and the effective barrier is  $\phi_b = 0.84 \pm 0.01$  eV. With six discrete deep defect states with the energy width of each state is 0.04 eV; the proposed model has a good agreement with experimental results.

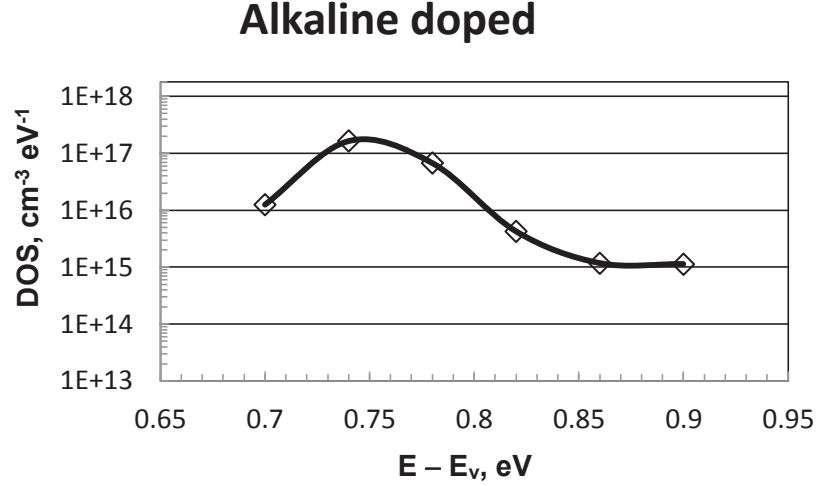


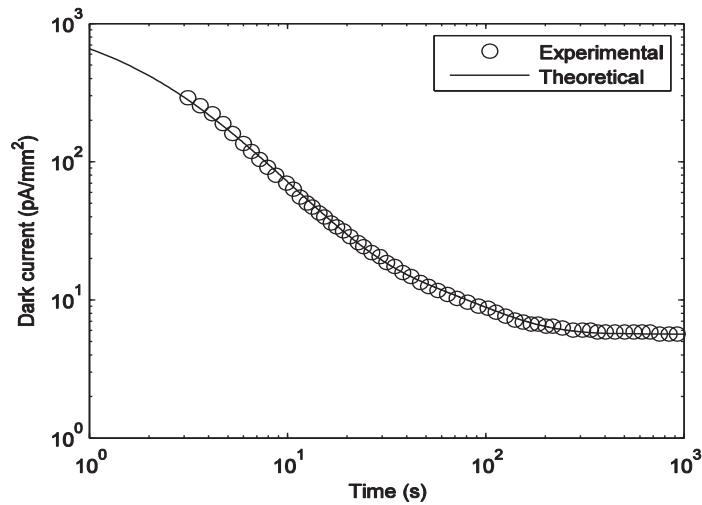
Figure 3.4: DOS distributions of deep states of n- alkaline doped n-layer by transient dark current analysis of Figs. 3.3

Figure 3.4 shows the defect densities versus energy (DOS). The peak defect states exist at 0.75 eV from the valance band mobility edge in alkaline doped *n*-layer which is much shallower than that of intrinsic a-Se (it is  $\sim 0.87$  eV deep in intrinsic a-Se [16].) Also the figure shows the existence of the deeper hole trapping states (up to 0.9 eV). The integrated concentration of deep defect states is  $\sim 10^{16}$  cm<sup>-3</sup>. Due to the presence of deeper hole trap states, the transient behavior is prolonged. That is why in the *n-i-p* sample dark current in any of the applied field does not reach a steady state value with in 1000 s.

### 3.4.2 The dark current in $n-i$ structure

The parameters of  $n$ - layer have dominant features controlling the dark current in multilayer a-Se detectors. So it is important to study the dark current behavior in  $n-i$  structures. Also the  $n$  layer of this structure is deposited at a low substrate temperature, which is below the glass transition temperature of the material. Such deposition is known as ‘cold deposition’. There are many advantages of cold deposition over the alkali deposited a-Se structures. The cold deposited  $n$ -layer has reduced hole transport with respect to  $i$ -layer, but has better electron transport than the doped  $n$ -layer [4]. At low substrate temperature, there is a decrement of hole-mobility lifetime product, but the electron life time remains unchanged.

Figure 3.5 shows the dark current density as a function of time for a cold deposited  $n-i$  structure. The symbols represent experimental data and the solid lines represent the theoretical fit to the experimental data. The experimental data have been extracted from figure 5 of reference [4]. To determine the energy distributed deep defect densities in  $n$ -layer, the deep defect states are discredited in six discrete states,  $E_{tm} = 0.7, 0.74, 0.78, 0.82, 0.86$  and  $0.9$  eV and the energy width of each state is  $0.04$  eV. The length of the  $n$  layer is  $L_n = 20$   $\mu\text{m}$  and  $L = 130$   $\mu\text{m}$ . The validated parameters are  $\omega_0 = 8 \times 10^{11}$  /s,  $\phi_b = 0.84$  eV. The integrated concentration of deep defect states is  $\sim 2.8 \times 10^{15}$   $\text{cm}^{-3}$ . Figure 3.5 shows a very good validity with the experimental result with the proposed model. The dark current reaches a plateau after approximately 600 s in the  $n-i$  structure.



**Figure 3.5:** Dark current density in an n-i structure as a function of time at  $10\text{V}/\mu\text{m}$  applied field. The symbol represents experimental data and the solid line represents the theoretical fit to the experimental data.

Figure 3.6 shows the defect densities versus energy (DOS). The peak defect states exist at  $0.78\text{ eV}$  from the valance band mobility edge in cold deposited *n*-layer which is much shallower than that of intrinsic a-Se. Also the figure shows the existence of the deeper hole trapping states (up to  $0.9\text{ eV}$ ) with a very low density.

From figure 3.4 and 3.6 it is observed that the total trap density in alkaline doped *n*-layer is higher than that in cold deposited *n*-layer.

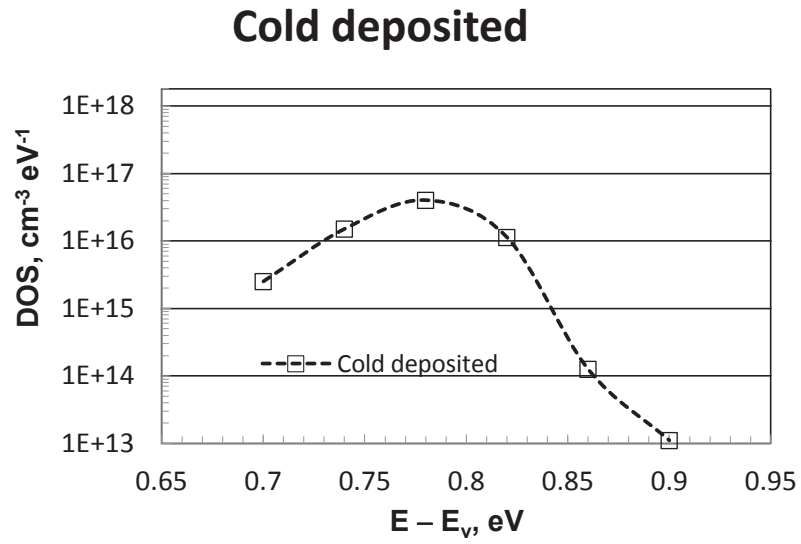


**Figure 3.6:** The DOS distributions of deep states in cold deposited n-layers by transient dark current analysis of Figure. 3.5.

### 3.4.3 The density of defect states:

Figure 3.7 shows the comparison of DOS of the alkaline doped *n-i-p* structure, cold deposited *n-i* structure and intrinsic a-Se. The differences among the DOSs are observed in terms of peak defect state level.

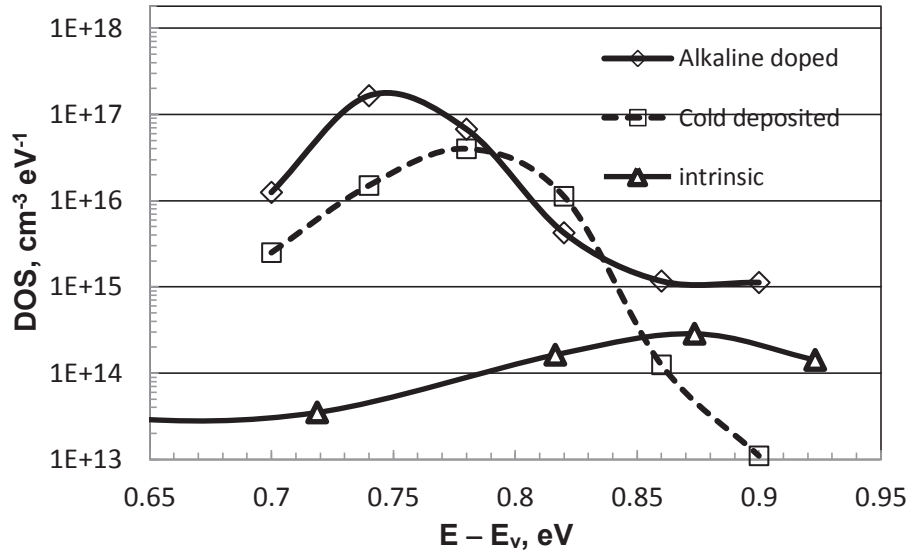


**Figure 3.7:** The DOS distributions of deep states for different  $n$  layers.

For the cold deposited  $n-i$  layer, a low defect density in the deeper states (0.85eV) is the main reason for the dark current to reach a plateau after approximately 600 s. The greater the density of the deep defect states, the longer the transient time. For  $n-i-p$  structure, deeper trap centers are responsible for longer transient behavior of the dark current. With a presence of a substantial amount of deep hole trapping states (up to 0.9 eV), the transient dark current does not reach the steady state within 1000 s as in  $n-i-p$  samples [5]. Therefore, the distribution of the defect density plays a vital role to explain the nature of the transient behavior of dark current.

To reduce the contact electric field and dark current, two points should be mentioned. Firstly, the  $n$ -layer must have sufficient amount of trap centers available so that a sufficient amount of injected holes get trapped. Secondly, the energy depth of these trap

centers should be  $\sim 0.75\text{-}0.8$  eV from the valance band mobility edge. Otherwise, if the trap centers are much shallower than this range then they are unable to retain sufficient amount of trap charges to reduce the dark current. On the other hand, if the trap centers are deeper, the transient time for the dark current would be longer and will take more time to reach the plateau. Therefore, an optimized dark current can be achievable if an abundant amount of trap centers with a energy depth of  $\sim 0.75\text{-}0.8$  eV from the valance band mobility edge are present in the hole blocking  $n$  layer.

### **3.5 Summary**

A dark current model for explaining transient and steady state dark current behaviors of multilayer  $\alpha$ -Se. X-ray imaging detectors has been described by considering energy distributed defect densities in the hole blocking layer ( $n$ -layer). The model is compared with recently published experimental transient dark currents on commercial  $n\text{-i-p}$  and cold deposited  $n\text{-i}$   $\alpha$ -Se detector structures and determined the energy distributed deep defect densities in these two types of  $n$ -layers. The energy depth of trap centers should be  $\sim 0.75\text{-}0.8$  eV from the valance band mobility edge for a requirement of low transient time to reach a plateau. The shallower trap levels are unable to retain sufficient amount of trap charges to reduce the dark current, and the deeper trap centers create longer transient time to reach a steady level of dark current.

## CHAPTER 4

### Dark current mechanism in avalanche a-Se detectors

With an excellent image quality in the field of digital mammography, a-Se has been a material in extensive research for last decades or so. Amorphous selenium based direct conversion X-ray detectors has potential perspective for many applications such as general radiography and fluoroscopy applications [35]. a-Se finds widespread use as an X-ray photoconductor due to its ability to be coated over a large area, its low dark conductivity and good carrier transport [36]. However, number of X-ray photon to convert into free EHP generation (conversion gain) is low compared to the other potential photoconductors such as polycrystalline mercuric iodide or lead oxide, makes a-Se unsuitable for low dose X-ray imaging. The overall noise can be higher than the signal strength in some parts of low dose imaging sensors. This severely affects the diagnostic features of that image. One extremely important attribute of a-Se is that it exhibits impact ionization, i.e., at a very high field  $F$  (above  $\sim 70\text{-}80\text{ V}/\mu\text{m}$ ) holes in a-Se can gain enough energy to create new EHPs through impact ionization with a useful avalanche gain of 1000 or more [24]. Thus avalanche multiplication may increase the signal strength and improve the signal to noise ratio in low dose X-ray imaging applications. However, dark current which is an important metric for X-ray detection also increases due to the the avalanche nature of the dark current.

As per our knowledge, no attempt has been made to investigate the sources of dark current in a-Se avalanche detector structures by physics-based quantitative modeling. In this chapter, a detailed analysis on quantitative dark current contributions from bulk thermal generation and carrier injections from the electrodes incorporating avalanche multiplication is performed. An analytical expression for the multiplication factors for various current components at the avalanche fields is derived. We compare the model with published experimental transient dark current at various fields to determine the magnitudes of various dark current components in different potential detector structures. The nature and relative importance of the injection and thermal generation currents are also examined in this thesis.

## **4.1 Different types of structures**

For avalanche a-Se detector different structures are investigated in literature [10],[37]. Among them three potential detector structures are considered in this thesis.

### **4.1.1 Type I structure**

As mentioned earlier, high electric field is necessary for the avalanche multiplication of X-ray generated charge. However, as the electric field profile is non-uniform at the edge of the metal electrode dielectric breakdown may occur. Once, breakdown occurs a huge amount of current can flow. As a result, there may be a phase transition and area near the electrode will become crystallized [37]. An introduction of new layer such as RIL (resistive interface layer) in the structure would help to avoid this irreversible breakdown

and making the stable a-Se avalanche pixilated imaging detector. With the presence of new layer there is evidence of improvement in stability as well as invulnerability of the dielectric at the metal electrode [37]. Although there is a possibility of interruption in charge transport in the a-Se/new layer contact, the time of flight (TOF) measurement ensures the a-Se transport properties do not degrade [37].

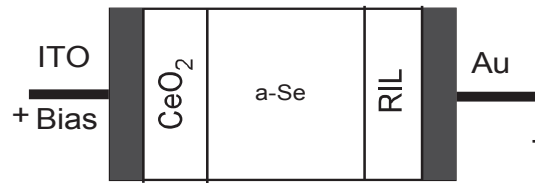
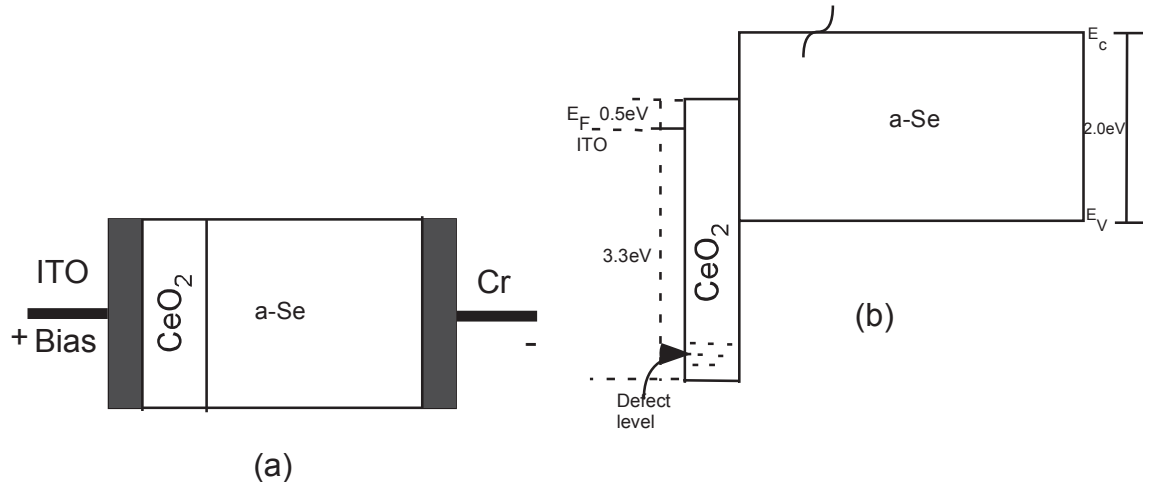


**Figure 4.1:** Schematic diagrams of a-Se avalanche detector structure (type I)

Figure 4.1 outlines the type I structure for the avalanche selenium detector. The device mainly consists of a-Se. The two blocking structures on the each side of the device prevent the injection of the charged carriers and suppress the dark current. Similar as HARP structure this structure also has  $\text{CeO}_2$  as a hole blocking layer. On the other hand,  $1\mu\text{m}$  thin resistive interface layer (RIL) is used as a electron blocking layer to avoid the break down. For top electrode Indium-tin-oxide (ITO) is used whereas bottom electrode Au is used.  $\text{CeO}_2$  has a thickness of  $\sim 10\text{-}30\text{nm}$ .  $\text{CeO}_2$  is an  $n$  type wide band gap ( $E_g \sim 3.3\text{ eV}$ ) material [9]. The thick RIL is made of a semi insulating polymer namely cellulose acetate (CA). RIL blocks the electron injection and prevents gold diffusion into a-Se structure [9]. This semi- insulating layer also has not effect on the transport properties of the a-Se and it prevents the initial breakdown.

### 4.1.2 Type II structure

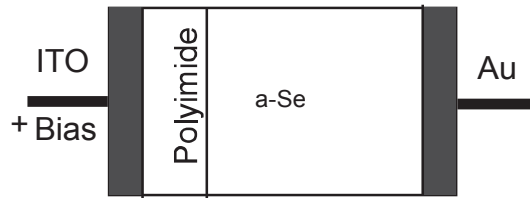
Figure 4.2 (a) outlines the type II structure for the avalanche selenium detector. This type II structure has  $\text{CeO}_2$  as only hole blocking layer.  $\text{CeO}_2$  has a thickness of  $\sim 10\text{-}30\text{nm}$  same as type I structure. For electron blocking there are no layers used. For top electrode Indium-tin-oxide (ITO) is used with Cr as a bottom layer is used.



**Figure 4.2 :**(a) Schematic diagrams of a-Se avalanche detector structure (type II) (b) Energy band diagram model of the hole blocking structure [10].

As there is no effective electron blocking layer there would be considerable amount of electron injection current. As a result transient state for dark current would be short. Figure 4.2(b) shows the energy band diagram of this structure. If many defect levels present near the top of the valance band, then due to the presence of defect level, the effective barrier height for hole blocking layer become less than the theoretical value. Therefore, hole injection from the metal/a-Se interface is not negligible.

### 4.1.3 Type III structure



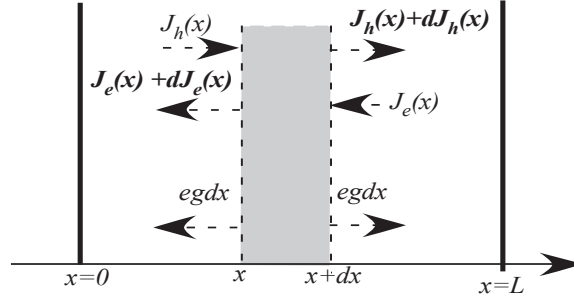
**Figure 4.3:** Schematic diagrams of a-Se avalanche detector structure (type III)

Figure 4.3 outlines the type III structure for the avalanche selenium detector. For this structure, polyimide (PI) is used as an organic material in this structure. PI is commonly used as an insulator and has a large band gap ( $\sim 7.1\text{eV}$ ). The following table sums up the three types of structures.

**Table 4.1** Comparisons of different parameters for various types of structures

Properties	Type I	Type II	Type III
Hole blocking layer	CeO <sub>2</sub> (~30nm)	CeO <sub>2</sub> (~30nm)	PI (800nm)
Electron blocking layer	resistive interface layer(RIL)	No blocking layer	No blocking layer
Anode(+Bias)	ITO	ITO	ITO
Cathode(+Bias)	Au	Cr	Au

## 4.2 The model for a-Se avalanche detector



**Figure 4.4:** Avalanche multiplication of holes and electrons under carrier injections and thermal generations  $L$  is the a-Se layer thickness.

Suppose that hole current density per unit area  $J_h(x)$  flows towards the right and electron current density  $J_e(x)$  flows toward the left as shown in figure 4.4. Due to impact ionization, holes create secondary generation of electron-hole pairs in avalanche field and there is also a net steady-state generation of EHPs of  $g$  per unit volume per unit time from the midgap defects near the Fermi level. As the field is very high and also a-Se layer is thin ( $<30 \mu\text{m}$ ) the charge collection efficiency in the a-Se detector is assumed to be unity [38]. Assuming negligible electron multiplication, the changes of hole and electron currents in  $dx$  per unit area are,

$$dJ_h(x) = \beta J_h(x) dx + egdx \quad (4.1)$$

$$dJ_e(x) = -\beta J_h(x) dx - egdx \quad (4.2)$$

Where  $e$  is the elementary charge and  $\beta$  is the impact ionization coefficient for holes. In equation (4.2), the  $J_h$  is the contribution of secondary electron due to the impact ionization of holes.

Rearranging the equation (4.1) we get,

$$\frac{dJ_h}{dx} - \beta J_h(x) = eg \quad (4.3)$$

$$J_h = C \exp(\beta x) - \frac{eg}{\beta}$$

Here is  $C$  is integration constant. So with the boundary conditions, considering hole injection current density,  $J_{h0}$  at  $x = 0$ , i.e.,  $J_h(x = 0) = J_{h0}$ , the constant term becomes

$$C = J_{h0} + \frac{eg}{\beta}$$

The solution of equation (4.1) would be

$$J_h(x) = J_{h0} \exp(\beta x) + \frac{eg}{\beta} [\exp(\beta x) - 1] \quad (4.4)$$

Similarly, rearranging equation (4.2) we get,

$$-\frac{dJ_e}{dx} = \beta J_h(x) + eg \quad (4.5)$$

Now substituting  $J_h(x)$  from equation (4.4) in equation (4.5) and after the integration we find,

$$J_e(x) = -J_{h0} \beta \left( \frac{\exp(\beta x)}{\beta} \right) - \frac{eg}{\beta} [\exp(\beta x)] + C1$$

Here is  $C1$  is integration constant. Again using the boundary condition, considering electron injection current density  $J_{e0}$  at  $x = L$  i.e.  $J_e(x = L) = J_{e0}$  the constant term becomes,

$$C1 = J_{e0} + J_{h0} \exp(\beta L) + \frac{eg}{\beta} [\exp(\beta L)]$$

Substituting the value of the constant term the solution of equation (4.2) becomes,

$$J_e(x) = J_{h0} [e^{\beta L} - e^{\beta x}] + \frac{eg}{\beta} [e^{\beta L} - e^{\beta x}] + J_{e0} \quad (4.6)$$

Finally, the dark current density due to injection and steady-state bulk thermal generation is [39]

$$J_{it} = J_e(x) + J_h(x)$$

$$J_{it} = J_{h0} \exp(\beta L) + \frac{eg}{\beta} [\exp(\beta L) - 1] + J_{e0} \quad (4.7)$$

The quantity  $J_{it}$  can be time-dependent if the injected current densities are time-dependent. Once the carriers are injected into the photoconductor layer, they move by drift mechanisms as diffusion component of current is negligible compared to its drift component in a-Se. Therefore, the injected current densities are

$$J_{e0} = e\mu_e F n_{inj} = e\mu_e F N_C \exp\left\{-\frac{\phi_e}{kT}\right\} \quad (4.8)$$

And,

$$J_{h0} = e\mu_h F N_v \exp\left\{-\frac{\phi_h}{kT}\right\} \quad (4.9)$$

where,  $n_{inj}$  is the average injected electron concentration from the bottom electrode,  $\mu$  is the effective drift mobility,  $T$  is the absolute temperature,  $k$  is the Boltzmann constant,  $F$  ( $\approx V/L$ ) is the applied field,  $V$  is the bias voltage,  $N_{V(C)}$  is the effective density of states in the valence (conduction) band, and  $\phi$  is the effective barrier height for injecting carriers from the electrode. The subscripts  $h$  and  $e$  stand for holes and electrons respectively. Here  $\phi$  is an adjustable parameter.

The avalanche multiplication factor  $\beta$  highly depends on the electric field and the a-Se layer thickness. This impact ionization coefficient is usually modeled by

$$\beta = A \exp \left[ - \left( \frac{B}{F} \right)^n \right]$$

where  $A, B, n$  are constants that depend on the semiconductor material properties. Value of  $n$  is a fitting parameter. Taking  $n \approx 1.0$  and other constant values of  $A$  and  $B$  the best fitted impact ionization coefficient follows the relation

$$\beta(F) = 1.1 \times 10^7 \exp \left( \frac{-1.09 \times 10^3}{F} \right) \text{ mm}^{-1} \quad (4.10)$$

The defect states close to the middle of the bandgap of a-Se have a high probability for thermal excitation of both types of carriers. Therefore, the steady-state thermal generation rate is dominated by the emission from traps within  $kT$  of steady state quasi-Fermi level  $E_{FD}$ . If the excitation rates for electrons and holes are equal,  $E_{FD}$  is very close to the middle of mobility gap. The generation rate for a fully depleted sample is determined by the average carrier release time and can be written as

$$g = N(E_{FD}) kT \omega_0 \exp \left[ - \left( E_C - E_{FD} - \beta_{pf} \sqrt{F} \right) / kT \right] \quad (4.11)$$

where,  $N(E_{FD})$  is the density of states of a-Se at energy  $E_{FD}$  in the midgap,  $\omega_0$  is the attempt-to-escape frequency,  $E_C$  is the conduction band edge,  $\beta_{pf} = \sqrt{e^3 / \pi \epsilon_{sr}}$  is the Poole-Frenkel coefficient and  $\epsilon_{sr}$  ( $=\epsilon_0 \epsilon_r$ ) is the permittivity of a-Se. It is assumed in equation (4.11) that the density of states is constant over  $kT$  near  $E_{FD}$ .

The bulk a-Se is slightly  $p$  type and thus there is a depletion of holes from the defect states near mid-gap after applying the bias. The Fermi level  $E_F$  in a-Se at zero bias is slightly below the mid-gap. The depletion of holes from the bulk and interface defect states within the mobility gap can constitute a transient dark current decay behavior. After applying the bias, holes are depleted and steady state quasi-Fermi level  $E_{FD}$  lies above  $E_F$ . The temporal behavior of the carrier depletion process is determined by the detrapping time constant. Therefore according to equation (4.6), the transient current density due to the hole depletion can be expressed as

$$J_{dp}(t) = J_{dpi}(t) \exp(\beta L) + \frac{J_{dpb}(t)}{\beta L} [\exp(\beta L) - 1] \quad (4.12)$$

where,

$$J_{dpi}(t) = e \int_{E_v}^{E_c} \frac{D_i(E)}{\tau_r(E)} \left[ \frac{1}{1 + \exp[(E - E_{FD})/kT]} - \frac{1}{1 + \exp[(E - E_F)/kT]} \right] \exp\left[-\frac{t}{\tau_{dy}(E)}\right] dE. \quad (4.13)$$

$$J_{dpb}(t) = \frac{e}{2L} \int_{E_v}^{E_c} \frac{N(E)}{\tau_r(E)} \left[ \frac{1}{1 + \exp[(E - E_{FD})/kT]} - \frac{1}{1 + \exp[(E - E_F)/kT]} \right] \exp\left[-\frac{t}{\tau_{dy}(E)}\right] dE. \quad (4.14)$$

with mean detrapping and carrier time constant,

$$\tau_r(E) = \omega_0^{-1} \exp\left[\frac{(E - \beta_{pf} \sqrt{F} - E_v)}{kT}\right] \quad (4.15)$$

$$\tau_{dy}(E) = \omega_0^{-1} \exp\left[\frac{(E - \gamma \beta_{pf} \sqrt{F} - E_v)}{kT}\right] \quad (4.16)$$

here  $t$  is the instantaneous time (in seconds),  $N(E)$  is the density of states of bulk a-Se at energy  $E$  in the mid-gap,  $D_i(E)$  is the density of interface states ( $\text{cm}^{-2}\text{eV}^{-1}$ ),  $E_v$  is the valance band edge, and  $\tau_r$  and  $\tau_{dy}$  are the mean detrapping and carrier decay time

constants.  $F = (V/L)$  is the applied field,  $V$  is the bias voltage and  $L$  is the layer thickness. The quantity  $\gamma$  is a free parameter and very close to one, which accounts for instantaneous carrier retrapping during depletion. Now the carrier mean detrapping and the carrier decay time constant will be same if  $\gamma = 1$ .

The total dark current density is the sum of all current components [39]

$$J_d(t) = J_{dp}(t) + J_{it}(t) \quad (4.17)$$

### 4.3 The result and discussion

The developed dark current model for avalanche a-Se detectors is compared with experimental reported transient dark decay curves at different fields in order to validate the dark current mechanisms presented in this chapter. The parameters,  $L = 15 \mu\text{m}$ ,  $\omega_0 = 7 \times 10^{11} / \text{s}$ ,  $N(E_{FD}) = 10^{15} \text{ cm}^{-3} \text{ eV}^{-1}$ ,  $\epsilon_r = 6.7$ ,  $N_C = N_V = 10^{19} / \text{cm}^3$ , and  $E_{FD} = E_g/2$  are taken in all calculations [39]. The room temperature effective hole drift mobility varies from  $\sim 0.25 \text{ cm}^2/\text{V-s}$  to  $0.85 \text{ cm}^2/\text{V-s}$  for the field variation of  $30 \text{ V}/\mu\text{m}$  to  $100 \text{ V}/\mu\text{m}$ . The electron drift mobility for the above fields varies from  $\sim 0.01 \text{ cm}^2/\text{V-s}$  to  $0.06 \text{ cm}^2/\text{V-s}$ . The room temperature for hole and electron drift mobility are taken from figure 3 of reference [37] and figure 3 of reference [40] respectively. Unless otherwise specified all the parameters mentioned above are fixed for all theoretical calculations in this thesis. Other parameters such as effective barrier height ( $\phi$ ) and mid-gap density of states  $N(E)$  depend on the fabrication processes and therefore, these are considered as adjustable parameters in the model.

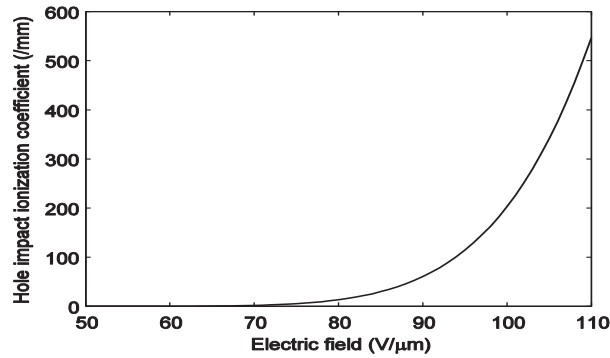


**Figure 4.5:** Impact ionization coefficient of holes as a function of electric field in a-Se.

The figure 4.5 shows the relationship of the hole impact ionization coefficient with the applied field. The impact ionization starts at the electric field of 70 V/μm and increases exponentially with field.

### 4.3.1 Type I structure

Figure 4.6 shows the transient dark current density in an avalanche a-Se detector structure (type I) for three different fields (30, 50 and 60 V/μm). The symbols represent experimental data, the dotted lines represent depletion and thermal generation current and the solid line represents the theoretical fit to the experimental data. The experimental data have been extracted from figure 5 of reference [37]. The a-Se layer thickness is 15μm. The proposed model shows a very good agreement with the experiment. The difference between the dotted line and solid lines represents the hole injection current.

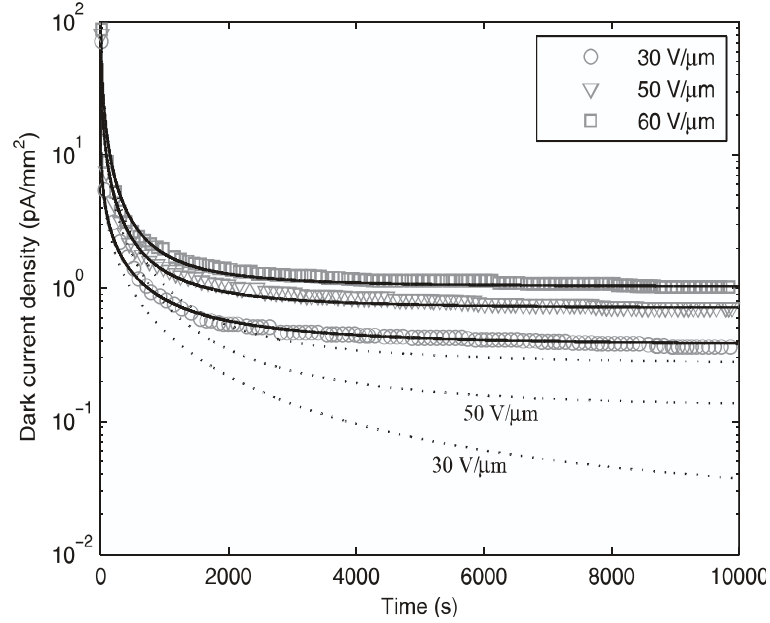


**Figure 4.6:** Dark current density versus time. The symbols represent experimental data and the solid lines represent the theoretical fits [39].

The electron injection from the bottom of the electrode is neglected as the  $1\mu\text{m}$  thick semi-insulating layer of RIL between the bottom electrode and a-Se. The  $\text{CeO}_2$  provides a theoretical barrier of  $\sim 2.8\text{eV}$  to the holes as shown in figure 4.2 (b). However the effective barrier can be much lower than this theoretical one because of many mid-gap defect levels near the valance band in  $\text{CeO}_2$  films [10]. The validated parameters are  $\omega_0=7\times 10^{11}/\text{s}$ ,  $\varphi_h=0.915\text{eV}$ ,  $N(E_{FD})=10^{15}\text{cm}^{-3}\text{eV}^{-1}$ ,  $D_i(E_{FD})=4\times 10^{13}\text{cm}^{-2}\text{eV}^{-1}$  and  $\gamma= 1.04$ ,  $0.95$  and  $0.91$  for the electric field of  $30, 50$  and  $60\text{ V}/\mu\text{m}$  respectively. There is a initial transient behavior within  $\sim 100\text{s}$ . This is due to the depletion of holes from the defect states near the mid-gap after applying the bias, which is approximately determined by the thermally detrapping time constant. From the figure 4.6 it is noticeable that the applied field is below the avalanche threshold ( $<70\text{V}/\mu\text{m}$ ). The fitting of the model with

experimental results determine the magnitudes of injection and bulk thermal generation currents.

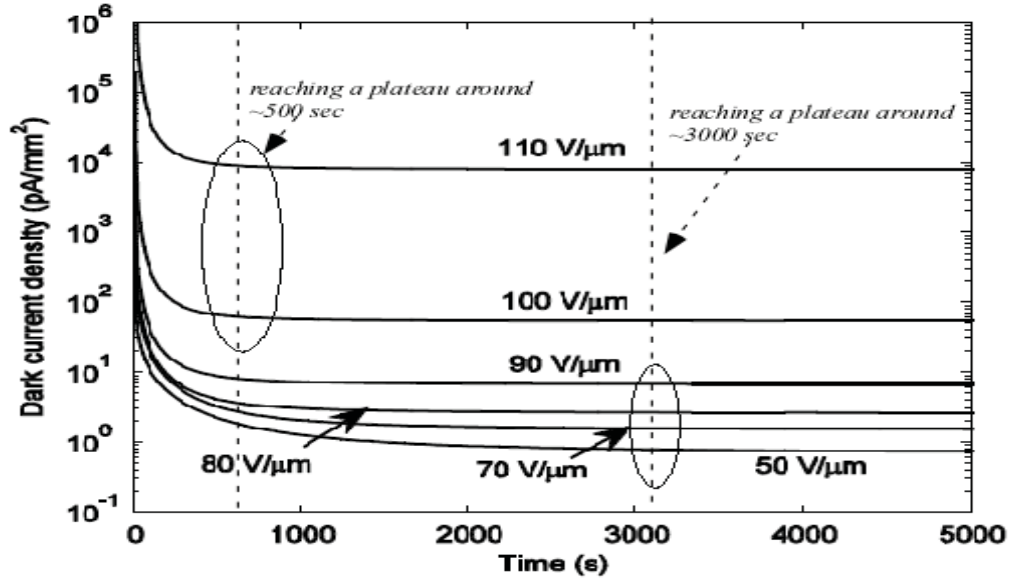


**Figure 4.7:** Dark current density versus time for the a-Se avalanche detector structure of Figure 4.6 at extremely high fields [39].

The dark current decay behaviors for the same detector (figure 4.6) at higher field are shown in figure 4.7. The dark current increases dramatically for the electric fields higher than  $80 \text{ V}/\mu\text{m}$  because of the avalanche multiplication. The dark current reaches a plateau after 3000 s at the electric field of  $50 \text{ V}/\mu\text{m}$ . However, it needs less than 500 s to reach the plateau at the field of  $110 \text{ V}/\mu\text{m}$  because of the faster release of depleted holes. As from the figure it is clear that the time required reaching the plateau decreases with increasing electric field and injection current.

The mobility gap of a-Se varies from 2.0 eV to 2.2 eV, and the thermal generation highly depends on the mobility gap. Figure 4.8 shows thermal generation current density versus electric field for varying mobility gap. The thermal generation current increases by almost one order of magnitude per 0.1 eV of reduction of mobility gap. Also, the thermal generation current increases sharply with increasing electric field

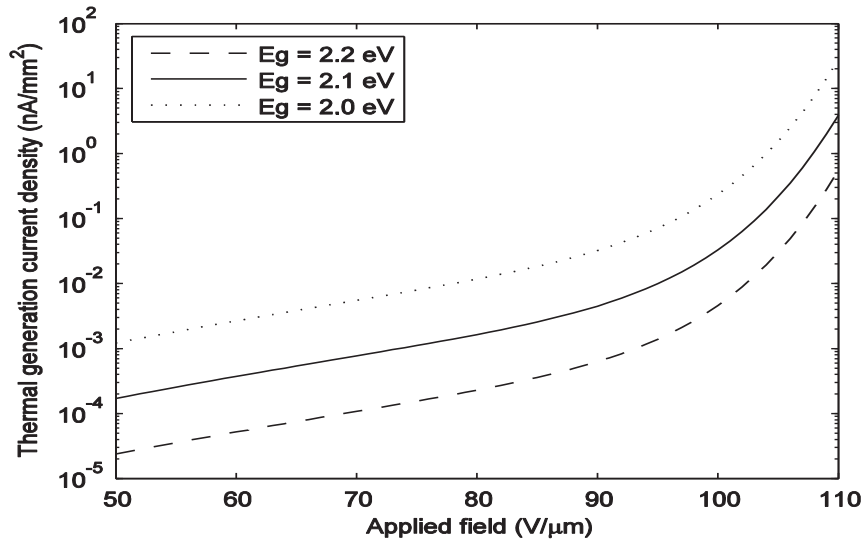
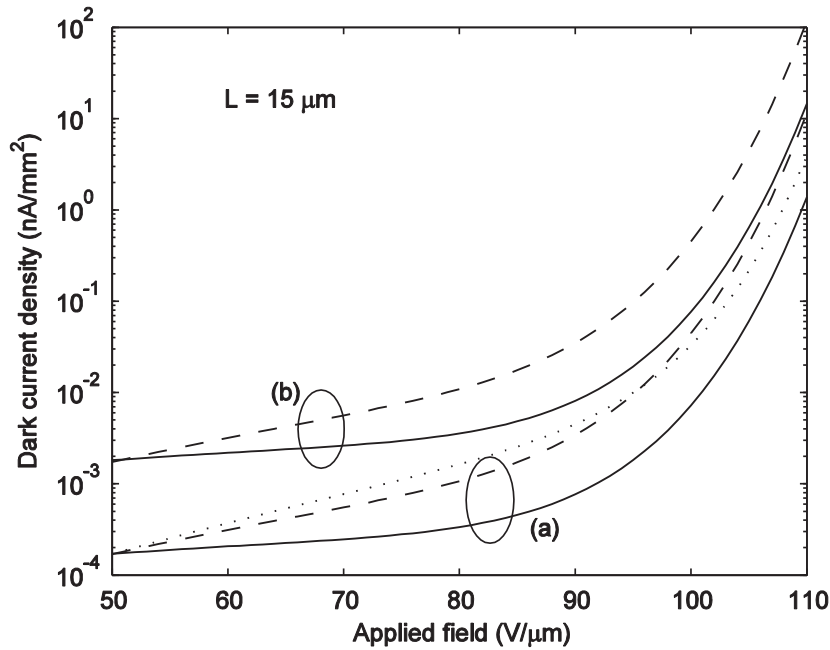


Figure 4.8: Thermal generation current density versus electric field for three different mobility gaps of a-Se.

The hole injection current is more critical than the electron injection current since the hole current undergoes avalanche multiplication process.

Figure 4.9 shows the thermal generation and hole injection current densities as a function of electric field. The dotted line represents the thermal generation current density for the mobility gap of 2.1 eV. The two sets of hole injection currents are; (a) equal to the thermal generation current at 50 V/μm, and (b) 10 times higher than the thermal

generation current at  $50 \text{ V}/\mu\text{m}$ . The dark current increases dramatically with increasing the field and a-Se thicknesses as shown in figure. 4.9. This work is extremely important to optimize the operating field and a-Se thickness for maximizing signal to noise ratio at the avalanche field operation of a-Se detector.



**Figure 4.9:** Hole injection current density as a function of electric field for (a) injection equal to thermal generation and, (b) injection equal to ten times thermal generation current at  $50 \text{ V}/\mu\text{m}$ . The dotted line represents the thermal generation current density for the mobility gap of  $2.1 \text{ eV}$ .

The effective barrier for holes from the top electrode can be much lower than the theoretical one because of many mid-gap defect levels near the valance band in dielectric hole blocking layer. The carrier transport in the dielectric hole blocking layer can follow Poole-Frenkel mechanisms. The solid and dashed lines represent hole injection current without and with Poole-Frenkel emission, respectively. The increase of injection current

is slower than that of thermal generation current below the avalanche threshold field ( $70 \text{ V}/\mu\text{m}$ ) and it is larger than that of thermal generation current past the avalanche threshold field. The impact of avalanche multiplication on the hole injection current is higher than that on the thermal generation current as evident from equation (4.7). The Poole-Frenkel effect lowers the potential barrier and enhances the injection current.

Figure 4.10 shows the steady-state dark current density as a function of electric field for two a-Se thicknesses.

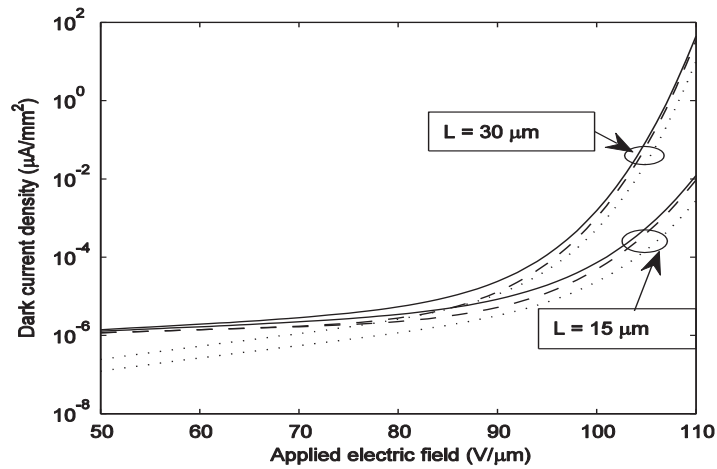


**Figure 4.10:** Dark current density as a function of electric field for two a-Se thicknesses. Dashed lines: hole injection current, dotted lines: bulk thermal generation current, and solid lines: total dark current.

The dashed lines represent the hole injection current, the dotted lines represent the bulk thermal generation current, and the solid lines represent the total dark current. The avalanche multiplication factor highly depends on the thickness of a-Se layer. All parameters in figure 4.10 are the same as in figure 4.6. Before the avalanche threshold

field ( $70 \text{ V}/\mu\text{m}$ ) the change in a-Se thicknesses is negligible. However after  $70 \text{ V}/\mu\text{m}$  the dark current increases with the increase of thickness of a-Se layer due to the avalanche multiplication factor.

### 4.3.2 The type II structure

Figure 4.11 shows the dark current density as a function of time for a type II a-Se avalanche detector at three different fields ( $15, 30$  and  $45 \mu\text{m}$ ). The symbols represent experimental data, and the solid line represents the theoretical results considering no tunneling when  $\alpha=0$  and dashed lines represent (when tunneling is  $1.3 \text{ nm}$ ) the theoretical results.

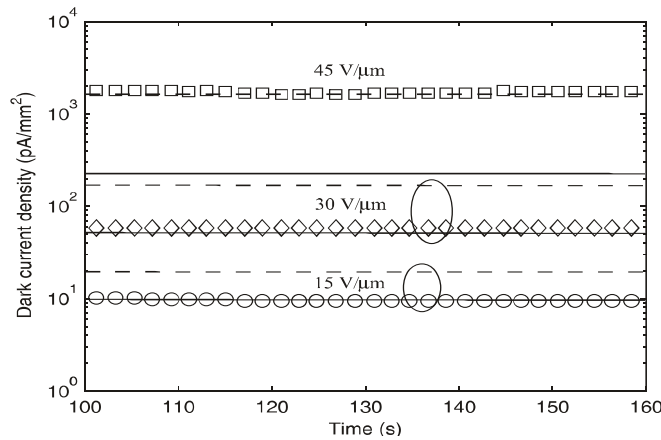


**Figure 4.11:** Dark current density versus time in type II a-Se avalanche detector structure for three different fields. Symbols: experimental data, and solid lines: theoretical data for no tunneling and dashed line for  $\alpha=1.3 \text{ nm}$  [39].

For this structure the fitted value is  $\phi_0=0.78 \text{ eV}$ . There is a considerable amount of electron injection current in type II structures because of no effective blocking layer. All parameters in figure 4.11 are the same as in figure 4.6. The validated effective barrier

height has both Schottky and thermally assisted tunneling components [32] i.e.

$$\varphi_e(F) = \varphi_0 - \sqrt{\frac{e^3 F}{4\pi\epsilon_s}} - \alpha F \text{ where } \varphi_0=0.78\text{eV and effective tunneling distance } \alpha=0\text{nm and}$$

1.3 nm. The experimental data has been extracted from reference [9] .The steady-state dark current in this structure is mainly controlled by huge electron injection current. The dark current reaches a plateau after approximately 100s because of very high injection current. Also fitting shows that effect of tunneling on the avalanche multiplication as for relatively lower fields (which is  $< 30\text{V}/\mu\text{m}$ ) the effective barrier lowering due to tunneling is mostly negligible whereas when the fields is very high as in this figure  $45\text{V}/\mu\text{m}$ , then even with a distance of nanometer range tunneling due to barrier lowering has a important impact.

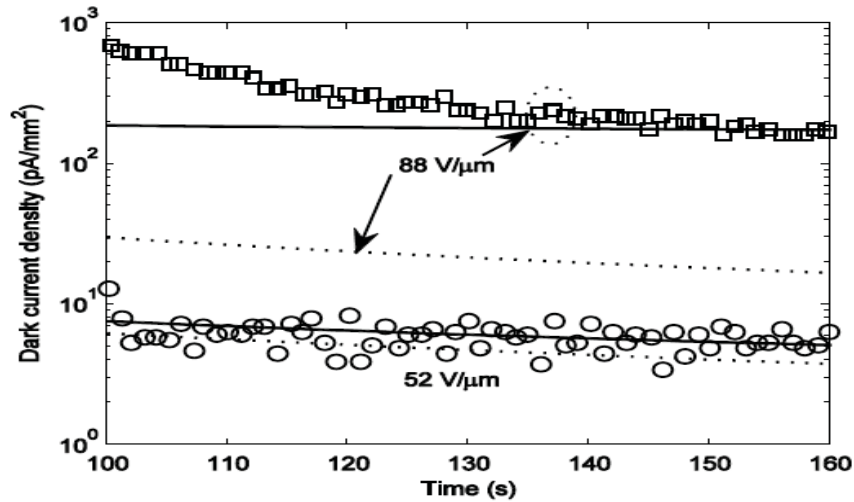
### 4.3.3 The type III structure

Figure 4.12 shows the dark current density as a function of time for type III a-Se avalanche detector at two different fields (52 and 88  $\text{V}/\mu\text{m}$ ). The symbols represent experimental data, dotted lines represent thermal generation and depletion current, and the solid line represent the theoretical fit to the experimental data. The experimental data has been extracted from figure 8 of reference [9]. Hole injection current is neglected in this structure because of high hole barrier created by polyimide layer. The validated

$$\text{barrier height for electron } \varphi_e(F) = \varphi_0 - \sqrt{\frac{e^3 F}{4\pi\epsilon_s}} \text{ where } \varphi_0=0.98\text{eV and effective}$$

tunneling distance  $\alpha=1.2\text{nm}$ . All parameters in figure 4.12 are the same as in figure

4.6. Here  $\gamma$  is taken within the range of 0.9-0.95. The difference between the dotted and the solid lines represents the electron injection current.



**Figure 4.12:** Dark current density versus time in type III a-Se avalanche detector structure for two different fields. Symbols: experimental data, dotted lines: thermal and hole injection current and solid lines: theoretical fit to the experimental data [39].

The electron injection current in type III structure is much lower than type II structure as evident from the difference between the electron barrier heights. The work function of Au (5.1eV) is higher than Cr (4.5eV). Therefore, Au should provide higher barrier than Cr, which is consistent with present results. The total dark current in type III structure is lower than that of type II structure because of negligible hole injection and lower electron injection.

## **4.4 Summary**

A physics based theoretical model for describing bias-dependent transient and steady-state dark current behaviors in amorphous Selenium (a-Se) avalanche detector structure has been described. The propose model is compared with published experimental results on three potential a-Se avalanche detector structures. The model shows a very good agreement with the experimental results. The steady-state dark current is the minimum for the structure that has effective blocking layers for both holes and electrons.

# CHAPTER 5

## Conclusion, Contribution and Future Work

### 5.1 Conclusion

In this thesis, an analytical model for explaining the variation of transient and steady state dark current behaviors of multilayer a-Se. X-ray imaging detectors has been described by considering energy distributed defect densities in the hole blocking layer (n-layer). Using the dark current analysis, a density of state for the alkaline doped *n-i-p* structure and cold deposited *n-i* layer based structure for X-ray detector has been analyzed This model has been validated with recently published experimental results. The simulation results have a good agreement with published results. The model elaborates the reason behind the variation of transient dark current in different samples. Also energy distributed defect densities helps to explain the optimal requirement for the performance. For a requirement of low transient time to reach a plateau, the energy depth of trap centers should be  $\sim 0.75$ - $0.8$  eV from the valance band mobility edge. If the trap levels are shallower then carriers will be unable to retain sufficient amount of trap charges from it. In that case the dark current will decay to a lower value. However, the deeper trap centers create longer transient time to reach a steady level of dark current. So for density of state of the hole

blocking layers helps out to explain this situation. Previously different models have been exploited with a two discrete deep trapping states in the hole blocking layer. In this model the deep trapping state has been distributed in six equal trapping states making the model more rigid. Also the DOS of the alkaline and cold deposited  $n$  layers are also observed with this developed dark current model.

In the second part of the thesis, an avalanche detector structure by physics-based quantitative modeling is developed. In this thesis, detailed analysis on quantitative dark current contributions from bulk thermal generation and carrier injections from the electrodes incorporating avalanche multiplication is performed. An analytical expression for the multiplication factors for various current components at the avalanche fields is also derived.

## 5.2 Contribution

The major contribution of this thesis are summarized as

- The density of states near valence band of hole blocking layer is determined by analyzing the transient dark current behaviors of multilayer a-Se X-ray imaging detectors. This analysis helps to obtain a low dark current and faster transient time to reach a plateau in these structures. The work on this analysis under the title **“Determination of density of defect states of n-type amorphous selenium in multilayer X-ray detectors”**, is submitted and accepted in **25th International**

### **Conference on Amorphous and Nano-crystalline Semiconductors conference**

which will be held on August 18-23, 2013 in Toronto, Canada

- A theoretical model for describing bias-dependent transient and steady-state behavior of dark current in a-Se avalanche detector structures has been developed. This analytical model considers bulk thermal generation current from mid-gap states, transient carrier depletion, and carrier injection from the electrodes incorporating avalanche multiplication. Also an analytical expression for the multiplication factors for various current components at the avalanche fields is derived. This work is published in *Applied Physics Letters* (DOI:10.1063/1.4802840) and in **proceeding of Nanotech conference & Expo 2013, Washington DC, USA.**

### **5.3 Future work**

The developed dark current model for practical a-Se multilayer detector can be examined under various X-ray exposures. More experimental work could be done on a-Se avalanche detectors for further observation. The signal to dark current ratio with variation the temperature or the exposure can be observed in different low dose imaging applications such as *fluoroscopy*. This could be a potential future work for this group.

## References:

- [1]. H. E. Johns and J. R. Cunningham, "The physics of radiology." 4th ed. Springfield, IL: Charles C Thomas, chap. 5 and 7, 1983
- [2]. S. O. Kasap and J. A. Rowlands, "Direct-conversion flat-panel X-ray image detectors," *IEE Proceedings: Circuits, Devices, and Systems*, vol. 149, no. 2, pp. 85-96, 2002
- [3]. J. A. Rowlands and J. Yorkston, "Flat panel detectors for digital radiography" in *Handbook of Medical Imaging*, vol. 1, J. Beutel, H. L. Kundel, and R. L. Van Metter, Ed. Washington: SPIE, , ch. 4, 2000
- [4]. S. O. Kasap, J. B. Frey, G. Belev, O. Tousignant, H. Mani, L. Laperriere, A. Reznik, and J. A. Rowlands, "Amorphous selenium and its alloys from early xeroradiography to high resolution X-ray image detectors and ultrasensitive imaging tubes," *Physica Status Solidi B*, vol. 246, no. 8, pp. 1794-1805, 2009
- [5]. S. A. Mahmood, M. Z. kabir, O. Tousignant, H. Mani, J. Greenspan, and P. Botka, "Dark current in multilayer amorphous selenium X-ray imaging detectors," *Applied Physics Letters*, vol. 92, no. 22, pp. 223506-1-3, 2008
- [6]. J. B. Frey, G. Belev, O. Tousignant, H. Mani, and S. O. Kasap, "Dark current in multilayer stabilized amorphous selenium X-ray photoconductors," *Physica Status Solidi C*, vol. 6, no. S1, pp. S251– S254, 2009
- [7]. D. C. Hunt, O. Tousignant, and J. A. Rowlands, "Evaluation of the imaging properties of an amorphous selenium-based flat panel detector for digital fluoroscopy," *Medical Physics*, vol. 31, no. 5, pp. 1166–1175, 2004
- [8]. J. B. Frey, G. Belev, O. Tousignant, H. Mani, L. Laperriere, and S. O. Kasap, "Dark current in multilayer stabilized amorphous selenium based photoconductive X-ray detectors," *Journal Applied Physics*, vol. 112, pp. 014502, 2012.
- [9]. K. Kikuchi, Y. Ohkawa, K. Miyakawa, T. Matsubara, K. Tanioka, M. Kubota, and N. Egami,"Hole-blocking mechanism in high-gain avalanche rushing

- amorphous photoconductor (HARP) film," *Physica Status Solidi C*, vol- 9,no-8, pp.2800-2803. 2011
- [10]. S.Abbaszadeh, N.Allec, S.Ghanbarzadeh, U.Shafique and Karim S. Karim, "Investigation of Hole-Blocking Contacts for High-Conversion-Gain Amorphous Selenium Detectors for X-ray Imaging," *IEEE transactions on Electron devices*, vol-59 pp. 9, 2012
- [11]. S. O. Kasap and G. Belev, "Progress in the science and technology of direct conversion X-ray image detectors: The development of a double layer a-Se based detector," *Journal of Optoelectronics and advanced materials*, vol. 9, no. 1, pp. 1–10, 2007
- [12]. S. O. Kasap, and J. A. Rowlands, "Direct-conversion flat-panel X-ray image sensors for digital radiography," *Proceedings of the IEEE*, vol. 90, no. 4, pp 591–604, 2002
- [13]. S. O. Kasap and J. A. Rowlands, "X-ray photoconductors and stabilized a-Se for direct conversion digital flat panel X-ray image detectors," *Journal of Materials Science: Materials in Electronics*, vol. 11, no. 3, pp. 179–198, 2000
- [14]. N.F. Mott, "Electrons in Disordered Structures," *Advances in Physics*, vol-16, pp.49-57, 1967
- [15]. A. E. Owen and J. M. Marshall, *Proceedings of the Seventh International Conference on Amorphous and Liquid Semiconductors, Edinburgh*, pp. 529, 1977
- [16]. M. Abkowitz, "Density of States in a-Se from Combined Analysis of Xerographic Potentials and Transient Transport Data," *Philosophical Magazine Letters*, vol - 58, pp. 53, 1988.
- [17]. S. O. Kasap, V. Aiyah, B. Polischuk, A. Bhattacharyya, and Z. Liang, "Deep-Trapping Kinematics of Charge Carriers in Amorphous Semiconductors: A Theoretical and Experimental Study," *Physical Review B*, vol 43, pp. 6691, 1991.
- [18]. K. V. Koughia, B. Fogal, G. Belev, R. E. Johanson, and S. O. Kasap, "Density of States in the Mobility Gap of Stabilized a-Se from Electron Time-of-Flight Photocurrent Analysis," *Journal of Non-Crystalline Solids*, vol-338, pp. 569, 2004.

- [19]. K. Koughia, Z. Shakoor, S. O. Kasap, and J. Marshall, "Density of Localized Electronic States in a-Se from Electron Time-of-Flight Photocurrent Analysis," *Journal of Applied Physics*, vol-97, pp.033706-1, 2005
- [20]. K. Koughia and S. O. Kasap, "Density of States of a-Se Near the Valence Band", *Journal of Non-Crystalline Solids*, vol-352, pp. 1539, 2006
- [21]. S. O. Kasap, K. V. Koughia, B. Fogal, G. Belev, and R. E. Johanson, "The Influence of Deposition Conditions and Alloying on the Electronic Properties of Amorphous Selenium," *Semiconductors*, vol-37, no-7, pp.789, 2003
- [22]. G. Belev, D. Tonchev, B. Fogal, C. Allen, and S. O. Kasap, "Effects of Oxygen and Chlorine on Charge Transport in Vacuum Deposited Pure a-Se Films," *Journal of Physics and Chemistry of Solids*, vol-68, pp. 972, 2007
- [23]. Afrin Sultana, Matthew M. Wronski, Karim S. Karim, and J. A. Rowlands, "Digital X-ray imaging using avalanche a-Se photoconductor," *IEEE Sensors Journal*, vol-10,pp.347-352,2010
- [24]. S. O. Kasap, J. A. Rowlands, S. D. Baranovskii, and Kenkichi Tanioka, "Lucky drift impact ionization in amorphous semiconductors," *Journal of applied physics*, vol-96, no. 4, pp- 2037-2048,2004
- [25]. Afrin Sultana, Alla Reznik, Karim S. Karim, and J. A. Rowlands, "Design and feasibility of active matrix flat panel detector using avalanche amorphous selenium for protein crystallography," *Medical physics*, vol-35, pp- 4324,2008
- [26]. M. Z. Kabir, S. O. Kasap, and J. A. Rowlands, in Springer Handbook of Electronic and photonic Materials, Ed. S. O. Kasap and Peter Capper (Springer, Heidelberg, 2006
- [27]. G. Belev, S. O. Kasap, J. A. Rowlands, D. Hunter, and M. Yaffe, "Dependence of the Electrical Properties of Stabilized a-Se on the Preparation Conditions and the Development of a Double Layer X-ray Detector Structure," *Current Applied Physics*, vol.3-4,no.8, pp. 383, 2008
- [28]. R. A. Street, "Thermal Generation Currents in Hydrogenated Amorphous Silicon p-i-n Structures," *Applied Physics Letters*, 57, pp. 1334, 1990

- [29]. R. A. Street, "Long-Time Transient Conduction in a-Si:H p-i-n Devices," *Philosophical Magazine B*, vol.63,no.6, pp. 1343, 1991
- [30]. R. E. Johanson, S. O. Kasap, J. Rowlands and B. Polischuk, "Metallic electrical contacts to stabilized amorphous selenium for use in X-ray image detectors," *Journal of Non Crystalline Solid*, vol. 227-230, pp. 1359-1362, 1998
- [31]. S. A. Mahmood, M. Z. Kabir, O. Tousignant, and J. Greenspan "Investigation of Ghosting Recovery Mechanisms in Selenium X-ray Detector Structures for Mammography", *IEEE Transaction on Nuclear Science*, vol. 59, pp. 597-604, 2012.
- [32]. E. Rosencher, V. Mosser, and G. Vincent, "Transient current study of field-assisted emission from shallow levels in silicon," *Physical review B*, vol. 29, pp. 1135, 1984
- [33]. H.-Z. Song, G. J. Adriaenssens, E. V. Emelianova, and V. I. Arkhipov, "Distribution of gap states in amorphous selenium thin films," *Physical Review B*, vol.59, pp.10607 ,1999
- [34]. G. E. Frank-Kamennetskaya, M. D. Vorontsov, and I. P. Kalinkin, "Electrical properties of film heterojunctions of cadmium selenide and amorphous selenium," *Soviet Physics Journal*, vol. 33, no. 11, pp. 952–957, Nov. 1990.
- [35]. S. O. Kasap et al. "Amorphous and Polycrystalline Photoconductors for Direct Conversion Flat Panel X-ray Image Sensors," *Sensors*, vol.11, pp.5112-5157, 2011
- [36]. M. Z Kabir, E. V. Emelianova, V. I. Arkhipov, M. Yunus, S. O. Kasap, and G. Adriaenssens, "The effects of large signals on charge collection in radiation detectors: Application to amorphous selenium detectors," *Journal of Applied Physics*, vol.99, pp.124501 ,2006
- [37]. O. Bubon, G. DeCrescenzo, J. A. Rowlands, Alla Reznik, "Amorphous selenium (a-Se) avalanche photosensor with metal electrodes," *Journal of Non-Crystalline Solids*, vol. 358, pp 2431-2433, 2012
- [38]. M. Z. Kabir, "Effects of charge carrier trapping on polycrystalline PbO X-ray imaging detectors," *Journal of Applied Physics*, vol. 104, pp-074506, 2008

- [39]. M. Z. Kabir and **Safayat-Al Imam** , "Transient and steady-state dark current mechanisms in amorphous selenium avalanche radiation detectors," *Applied Physics Letters*, vol.102, pp-153515, 2013
- [40]. G. Juška, K. Arlauskas, "Impact ionization and mobilities of charge carriers at high electric fields in amorphous selenium," *Physica status solidi (a)*, vol. 59, pp.389–393, 1980